

Bayesian Inference of Fine-Features of Nuclear Equation of State from Future Neutron Star Radius Measurements to 0.1km Accuracy

Bao-An Li^{1*}, Xavier Grundler^{1†}, Wen-Jie Xie^{1,2,3‡}, and Nai-Bo Zhang^{1,4§}

¹*Department of Physics and Astronomy, Texas A&M University-Commerce, Commerce, TX 75429-3011, USA*

²*Department of Physics, Yuncheng University, Yuncheng 044000, China*

³*Guangxi Key Laboratory of Nuclear Physics and Nuclear Technology, Guangxi Normal University, Guilin 541004, China and*

⁴*School of Physics, Southeast University, Nanjing 211189, China*

(Dated: July 11, 2024)

To more precisely constrain the Equation of State (EOS) of supradense neutron-rich nuclear matter, future high-precision X-ray and gravitational wave observatories are proposed to measure the radii of neutron stars (NSs) with an accuracy better than about 0.1 km. However, it remains unclear what particular aspects (other than the stiffness generally spoken of in the literature) of the EOS and to what precision they will be better constrained. In this work, within a Bayesian framework using a meta-model EOS for NSs, we infer the posterior probability distribution functions (PDFs) of incompressibility K_0 and skewness J_0 of symmetric nuclear matter (SNM) as well as the slope L , curvature K_{sym} , and skewness J_{sym} characterizing the density dependence of nuclear symmetry energy $E_{\text{sym}}(\rho)$, respectively, from mean values of NS radii consistent with existing observations and an expected accuracy ΔR ranging from about 1.0 km to 0.1 km. We found that (1) the ΔR has little effect on inferring the stiffness of SNM at suprasaturation densities, (2) smaller ΔR reveals more accurately not only the PDFs but also pairwise correlations among parameters characterizing high-density $E_{\text{sym}}(\rho)$, (3) a double-peak feature of the PDF(K_{sym}) corresponding to the strong $K_{\text{sym}} - J_{\text{sym}}$ and $K_{\text{sym}} - L$ anti-correlations is revealed when ΔR is less than about 0.2 km, (4) the high-precision radius measurement for canonical NSs is more useful than that for massive ones for constraining the EOS of nucleonic matter around (2-3) times the saturation density of SNM.

PACS numbers:

I. INTRODUCTION

Neutron stars (NSs) are natural testing grounds for our knowledge about the nature and Equation of State (EOS) of supradense neutron-rich matter, see, e.g., Refs.[1–8]. In particular, the radii of canonical NSs of masses around $1.4 M_\odot$ carry important information about the EOS, especially its symmetry energy term, at densities around twice the saturation density ρ_0 of symmetric nuclear matter (SNM) [9]. While much progress has been made, especially since GW170817, measuring precisely the radii of NSs has been extremely challenging. Some surveys of extensive analyses of X-rays and gravitational waves in the recent literature indicate that the mean radius of a canonical NS is about $R_{1.4} = 12.0 \pm 1.13$ km at 68% credibility assuming all reports are equally reliable [10], and empirically $R_{1.4} \approx R_{1.8} \approx R_{2.0}$ within about 1.0 km precision [11]. While the available NS observational data have improved our understanding of dense matter EOS, more precise radius measurements are considered a critical task for making further progress. Indeed, high-precision NS radius measurements have been identified by the astrophysics community as a major science

driver of the next-generation X-ray pulse profile observatories, e.g., The enhanced X-ray Timing and Polarimetry mission (eXTP) [12], Spectroscopic Time-Resolving Observatory for Broadband Energy X-rays (STROBE-X) [13], and third-generation gravitational-wave detectors [14, 15], e.g., Einstein Telescope [16] and Cosmic Explorer [17]. Based on several recent analyses and simulations, see, e.g., Refs. [18–22], the planned new facilities can measure the $R_{1.4}$ to a precision better than 2.0%. For example, considering only the 75 loudest events of the expected more than 3×10^5 binary NS mergers in the one-year operation of a network consisting of one Cosmic Explorer and the Einstein Telescope, the radii of NSs in the mass range (1-1.97) M_\odot will be constrained to at least $\Delta R \leq 0.2$ km at 90% credibility [22]. It was also pointed out that a single 40 km Cosmic Explorer detector can pin down the NS radius to an accuracy of 10 meters within a decade, whereas the current generation of ground-based detectors like the Advanced LIGO-Virgo network would take $\mathcal{O}(10^5)$ years to do so [20].

Certainly, there is no doubt that measuring precisely the radii of NSs is scientifically invaluable, especially for resolving many mysteries associated with NSs and the EOS of the densest visible matter in the universe. On the other hand, given the extreme difficulties and the required super-expensive investments in several measures, thoroughly investigating the scientific returns in multiple areas from such measurement is also invaluable and probably a prerequisite. Acknowledging *a priori* that probably many important new physics that can

*Corresponding Author: Bao-An.Li@Tamuc.edu

†xgrundler@leomail.tamuc.edu

‡wenjixie@yeah.net

§naibozhang@seu.edu.cn

be discovered from the proposed high-precision NS radius measurements is beyond the current knowledge of the authors, here we focus on investigating what the proposed high-precision radius measurements will teach us about the EOS of supradense neutron-rich nucleonic matter within the minimum model of NSs consisting of neutrons, protons, electrons, and muons ($npe\mu$) at β -equilibrium. Such NS EOS is the most fundamental basis for constructing more complicated EOS models considering more degrees of freedom and possible phase transitions. Since going beyond the minimum NS EOS model inevitably involves more assumptions and uncertainties, our study here can thus be considered the most conservative one. Of course, we can not exclude any physics associated with new particles beyond $npe\mu$ and/or possible phase transitions in NSs.

In the literature, there are general speculations on how the high-precision radius measurements may constrain the stiffness of supradense NS matter EOS. However, it is presently unclear which particular features of the EOS and to what extent they can be more precisely constrained compared to our current best knowledge. To fill this knowledge gap, in this work, we infer the PDFs of parameters characterizing the density dependence of both SNM EOS and nuclear symmetry energy within a Bayesian framework. As discussed in detail in Ref. [9], because the NS radius R is determined by the radial coordinate where the pressure vanishes, R scales with the pressure around $(1 - 2)\rho_0$ [9] and is thus most sensitive to the EOS of neutron-rich matter around $2\rho_0$. Contributions to the pressure around this density from SNM EOS and nuclear symmetry energy compete strongly depending on the values of L , K_{sym} , and J_0 [23, 24]. More specifically, using machine learning techniques to large sets of posterior EOS parameters from Bayesian analyses of existing NS radius data, it was found earlier that the most important EOS parameters determining $R_{1.4}$ are (in order of decreasing importance): curvature K_{sym} , slope L , skewness J_{sym} of nuclear symmetry energy, skewness J_0 , incompressibility K_0 of symmetric nuclear matter, and the magnitude $E_{\text{sym}}(\rho_0)$ of symmetry energy at the saturation density ρ_0 of nuclear matter [25]. Thus, the radii of canonical NSs are expected to be most useful for constraining the EOS of neutron-rich matter around $2\rho_0$ instead of the much higher core densities, and we have no reason to believe the radii (but the masses themselves) of massive NSs are more useful than those of canonical ones for this purpose. In this work, we shall study how the PDFs and pairwise correlations of these EOS parameters may be altered by using mean values of NS radii consistent with existing observations and varying the accuracy ΔR from about 1.0 km to 0.1 km. These results are useful for further developing and constraining nuclear many-body theories for supradense neutron-rich nuclear matter [6, 7]. They also provide useful guidance and reference for laboratory tests of these EOS parameters using heavy-ion reactions induced by high-energy radioactive beams [26–28].

The rest of the paper is organized as follows. In the next section, we shall first outline the meta-model EOS for NS matter, the Bayesian statistical framework we employ and the existing NS radius data that we use as a basis for our study with expected future precision. In section III, we present and discuss our results. Finally, a summary is given.

II. THEORETICAL FRAMEWORK: META-MODEL EOS AND BAYESIAN APPROACH

For completeness and ease of our discussions, we recall in the following several main aspects of our approach. More technical details and examples of applications can be found in our earlier publications (e.g. [29–34]) and reviews [5, 35].

A. Explicitly isospin-dependent meta-model EOS for neutron stars

A meta-model is a model of models. We construct an NS meta-model that can mimic all existing EOSs for $npe\mu$ matter at β -equilibrium. It is based on parameterizing the binding energy per nucleon $E(\rho, \delta)$ in neutron-rich matter at nucleon density $\rho = \rho_n + \rho_p$ and isospin asymmetry $\delta \equiv (\rho_n - \rho_p)/\rho$ [36]

$$E(\rho, \delta) = E_0(\rho) + E_{\text{sym}}(\rho) \cdot \delta^2 + \mathcal{O}(\delta^4) \quad (1)$$

where $E_0(\rho)$ is the SNM EOS and $E_{\text{sym}}(\rho)$ is nuclear symmetry energy at density ρ . The pressure in NSs is obtained from

$$P(\rho, \delta) = \rho^2 \frac{d\epsilon(\rho, \delta)/\rho}{d\rho}, \quad (2)$$

where $\epsilon(\rho, \delta) = \epsilon_n(\rho, \delta) + \epsilon_l(\rho, \delta)$ is the energy density of NS matter. Here, $\epsilon_n(\rho, \delta)$ and $\epsilon_l(\rho, \delta)$ are the energy densities of nucleons and leptons, respectively. The energy density of leptons, $\epsilon_l(\rho, \delta)$, is determined using the noninteracting Fermi gas model [37]. On the other hand, the energy density of nucleons, $\epsilon_n(\rho, \delta)$, is linked to the $E(\rho, \delta)$, and the average mass M_N of nucleons via

$$\epsilon_n(\rho, \delta) = \rho[E(\rho, \delta) + M_N]. \quad (3)$$

The density profile of isospin asymmetry $\delta(\rho)$ is obtained by using the β -equilibrium condition $\mu_n - \mu_p = \mu_e = \mu_\mu \approx 4\delta E_{\text{sym}}(\rho)$ and the charge neutrality requirement $\rho_p = \rho_e + \rho_\mu$. Here the chemical potential μ_i for a particle i is calculated from the energy density via $\mu_i = \partial\epsilon(\rho, \delta)/\partial\rho_i$. With the above $\delta(\rho)$, both the pressure $P(\rho, \delta(\rho))$ and energy density $\epsilon(\rho, \delta(\rho))$ become barotropic, i.e., depending on density only. The core EOS described above is then connected with the crust EOS at a transition density consistently determined by

examining when the core EOS becomes thermodynamically unstable [38–40]. We adopt the Negele-Vautherin (NV) EOS [41] for the inner crust and the Baym-Pethick-Sutherland (BPS) EOS [42] for the outer crust. Finally, the complete NS EOS in the form of pressure versus energy density $P(\epsilon)$ is used in solving the Tolman-Oppenheimer-Volkoff (TOV) equations [37, 43].

TABLE I: Prior ranges of the six EOS parameters (MeV).

Parameters	Lower limit	Upper limit
K_0	220	260
J_0	-400	400
K_{sym}	-400	100
J_{sym}	-200	800
L	30	90
$E_{\text{sym}}(\rho_0)$	28.5	34.9

The $E_0(\rho)$ and $E_{\text{sym}}(\rho)$ can be parameterized as

$$E_0(\rho) = E_0(\rho_0) + \frac{K_0}{2} \left(\frac{\rho - \rho_0}{3\rho_0} \right)^2 + \frac{J_0}{6} \left(\frac{\rho - \rho_0}{3\rho_0} \right)^3, \quad (4)$$

$$E_{\text{sym}}(\rho) = E_{\text{sym}}(\rho_0) + L \left(\frac{\rho - \rho_0}{3\rho_0} \right) + \frac{K_{\text{sym}}}{2} \left(\frac{\rho - \rho_0}{3\rho_0} \right)^2 + \frac{J_{\text{sym}}}{6} \left(\frac{\rho - \rho_0}{3\rho_0} \right)^3, \quad (5)$$

where $E_0(\rho_0) = -16$ MeV at $\rho_0 = 0.16/\text{fm}^3$. The coefficients K_0 and J_0 defined as

$$K_0 = 9\rho_0^2 [\partial^2 E_0(\rho) / \partial \rho^2] |_{\rho=\rho_0}, \quad (6)$$

$$J_0 = 27\rho_0^3 [\partial^3 E_0(\rho) / \partial \rho^3] |_{\rho=\rho_0} \quad (7)$$

are the SNM incompressibility and skewness, respectively. The $E_{\text{sym}}(\rho_0)$,

$$L = 3\rho_0 [\partial E_{\text{sym}}(\rho) / \partial \rho] |_{\rho=\rho_0}, \quad (8)$$

$$K_{\text{sym}} = 9\rho_0^2 [\partial^2 E_{\text{sym}}(\rho) / \partial \rho^2] |_{\rho=\rho_0}, \quad (9)$$

$$J_{\text{sym}} = 27\rho_0^3 [\partial^3 E_{\text{sym}}(\rho) / \partial \rho^3] |_{\rho=\rho_0} \quad (10)$$

are the magnitude, slope, curvature and skewness of nuclear symmetry energy at ρ_0 , respectively. While these coefficients are all defined at ρ_0 , the high-order derivatives characterize the high-density behaviors of $E_0(\rho)$ and $E_{\text{sym}}(\rho)$, respectively. In particular, the skewness parameters J_0 and J_{sym} characterize the stiffness of $E_0(\rho)$ and $E_{\text{sym}}(\rho)$ around $(3 - 4)\rho_0$ [44], and K_{sym} characterizes the stiffness of $E_{\text{sym}}(\rho)$ around $(2 - 3)\rho_0$. In our meta-model EOS used in the Bayesian framework, these coefficients are randomly generated in their prior uncertainty ranges listed in Table I [10] in each Markov-Chain Monte Carlo (MCMC) step. These uncertainty ranges are based on the knowledge the community has accumulated over the last 40 years from analyzing terrestrial experiments, astrophysical observations, and extensive theoretical studies. In particular, $E_0(\rho_0)$ and K_0 have been relatively well constrained respectively to $E_0(\rho_0) =$

-15.9 ± 0.4 MeV and $K_0 = 240 \pm 20$ MeV [45, 46]. Similarly, $E_{\text{sym}}(\rho_0) = 31.7 \pm 3.2$ MeV and $L = 58.7 \pm 28.1$ MeV at 68% confidence level [47–49], respectively. While the parameters characterizing the isospin-asymmetric EOS at suprasaturation densities, i.e., $K_{\text{sym}} = -100 \pm 100$ MeV [5, 50–53], $J_0 = -190 \pm 100$ MeV [30, 32, 33, 44], and $-200 < J_{\text{sym}} < 800$ MeV [54–56], still have rather large errors.

In comparison with many NS EOS models in the literature, two features of the meta-model EOS described above deserve emphasizing:

1. It is well known that the TOV equations are degenerate about the compositions of NSs (i.e., composition blind) in the sense that once the EOS $P(\epsilon)$ is given, the mass-radius sequence is uniquely determined regardless of how the $P(\epsilon)$ is constructed or what particles/phases are considered. At suprasaturation densities, since there is presently no completely reliable theory, one often parameterizes directly the $P(\epsilon)$ using piecewise polytropes or spectrum functions [57]. These types of parameterizations, however, carry no non-degenerate information about NS composition. They can not be used to reveal the underlying nuclear symmetry energy which is presently the most uncertain term in the EOS of supradense neutron-rich nucleonic matter but most important for determining the radii of NSs and/or the cooling mechanisms of protoneutron stars [58]. Our meta-model EOS is built from a more fundamental level with NS composition determined self-consistently by the density dependence of nuclear symmetry energy. It has the same flexibility as the piecewise polytropes by varying the EOS parameters within their prior ranges constrained by existing nuclear laboratory data and theoretical predictions. On the contrary, there is little direct experimental or prior information about parameters describing especially the high-density pieces of the polytropical EOSs.
2. On the other hand, compared to the microscopic and/or phenomenological nuclear many-body theories for NS matter, our meta-model EOS is not so fundamental or microscopic enough for some purposes. Nevertheless, it can mimic most EOSs predicted by these many-body theories. Most importantly, it provides the flexibility and diversity necessary for the purposes of this work in a Bayesian statistical framework.
3. The parameterizations for $E_0(\rho)$ and $E_{\text{sym}}(\rho)$ look like Taylor expansions for known energy density functionals. Indeed, the EOS parameters asymptotically become the coefficients of the Taylor expansions as $\rho \rightarrow \rho_0$. Here, they are just parameters to be inferred from the observational/experimental data instead of expanding some known energy den-

sity functionals [59]. The issue of convergence associated with Taylor expansions does not exist in our Bayesian analyses. Moreover, the last parameters, i.e. J_0 and J_{sym} , carry all information about the high-density EOS of neutron-rich matter. In Bayesian analyses, once the EOS parameters are randomly generated within their prior ranges in each MCMC step, the NS EOS can be constructed as described above.

B. Bayesian inference approach

For completeness, we recall that the Bayesian theorem reads

$$P(\mathcal{M}|D) = \frac{P(D|\mathcal{M})P(\mathcal{M})}{\int P(D|\mathcal{M})P(\mathcal{M})d\mathcal{M}}. \quad (11)$$

Here $P(\mathcal{M}|D)$ represents the posterior probability of the model \mathcal{M} (described here by the 6 meta-model EOS parameters) given the dataset D . Meanwhile, $P(D|\mathcal{M})$ is the likelihood function that a given theoretical model \mathcal{M} predicts the data D , and $P(\mathcal{M})$ is the prior probability of the model \mathcal{M} before encountering its prediction with the given data. The denominator in Eq. (11) is a normalization constant.

TABLE II: Neutron star data used in the present work. For the radii of the four millisecond pulsars (MPSs), the uncertainties correspond to approximately (5-10)% constraints on R with the extent in M corresponding to the 1σ bounds from the radio measurements [1].

Mass(M_{\odot})	Radius R (km)	Source and Reference
1.4	$11.9_{-1.4}^{+1.4}$ (90% CFL)	GW170817[60]
1.4	$10.8_{-1.6}^{+2.1}$ (90% CFL)	GW170817 [61]
1.4	$11.7_{-1.1}^{+1.1}$ (90% CFL)	QLMXBs [62]
$1.34_{-0.16}^{+0.15}$	$12.71_{-1.19}^{+1.14}$ (68% CFL)	PSR J0030+0451 [63]
$1.44_{-0.14}^{+0.15}$	$13.0_{-1.0}^{+1.2}$ (68% CFL)	PSR J0030+0451 [64]
$2.08_{-0.07}^{+0.07}$	$13.7_{-1.5}^{+2.8}$ (68% CFL)	PSR J0740+6620 [65]
$1.26_{-0.14}^{+0.14}$	$12.28_{-0.45}^{+0.45}$	MSP J0751+1807 [1, 66]
$1.54_{-0.03}^{+0.03}$	$11.57_{-0.56}^{+0.56}$	MSP J1909+3744 [1, 67]
$1.831_{-0.01}^{+0.01}$	$12.53_{-0.57}^{+0.57}$	MSP J2222+0137 [1, 68]
$1.908_{-0.016}^{+0.016}$	$11.93_{-0.50}^{+0.50}$	MSP J1614+2230 [1, 69]

We randomly sample uniformly the six EOS parameters within their prior ranges specified by their minimum and maximum values given in Table I. For each set of the EOS parameters, we construct the NS EOS at β -equilibrium as described earlier. The corresponding NS mass-radius sequence is determined by solving the TOV equations. The resultant theoretical radius $R_{\text{th},j}$ is then utilized to assess the likelihood of the selected EOS parameter set to reproduce the observed radius $R_{\text{obs},j}$, where j ranges from 1 to the total number N of radius data used in the particular analysis. This radius likeli-

hood is calculated from

$$P_{\text{R}}[D(R_{1,2,\dots,N})|\mathcal{M}(p_{1,2,\dots,N})] = \prod_{j=1}^N \frac{1}{\sqrt{2\pi}\sigma_{\text{obs},j}} \exp\left[-\frac{(R_{\text{th},j} - R_{\text{obs},j})^2}{2\sigma_{\text{obs},j}^2}\right], \quad (12)$$

where $\sigma_{\text{obs},j}$ represents the 1σ error bar associated with the observation j . If there is more than one analysis for the same NS, e.g., the independent analyses using somewhat different approaches of the same observational data by NICER Collaboration, we treat them as equally reliable within the error bars published.

Depending on the purpose of each analysis, the total likelihood function can be constructed differently by selecting and multiplying the individual likelihood components. Our base/default total likelihood function is given by

$$P(D|\mathcal{M})_{\text{base}} = P_{\text{filter}} \times P_{\text{mass,max}} \times P_{\text{R}}. \quad (13)$$

Here, P_{filter} and $P_{\text{mass,max}}$ indicate that the generated EOSs must satisfy the following conditions: (i) The crust-core transition pressure remains positive; (ii) The thermodynamic stability condition, $dP/d\epsilon \geq 0$, holds at all densities; (iii) The causality condition is upheld at all densities; (iv) The generated NS EOS should be sufficiently stiff to support NSs at least as massive as $1.97 M_{\odot}$ as in the original analysis of GW170817 by the LIGO/VIRGO Collaborations [70].

For this work, we use the mean or most probable radii of several NSs listed in Table II but vary their precision $\Delta R = \sigma_{\text{obs},j}$. In particular, we consider the following cases:

1. A single canonical NS with $R_{1.4} = 11.9$ km as inferred by the LIGO/VIRGO Collaborations from GW170817 [70] with $\Delta R = 1.0, 0.5, 0.2$, and 0.1 km, respectively.
2. Three canonical NSs with $R_{1.4} = 11.8, 11.9$ and 12.0 km, respectively, all with $\Delta R = 0.1$ km.
3. A single NS with a mass of $2.0M_{\odot}$ and $R_{2.0} = 11.9$ km with $\Delta R = 1.0, 0.5, 0.2$, and 0.1 km, respectively.
4. Four NSs with a mass of $1.4, 1.6, 1.8$ and $2.0M_{\odot}$, respectively, all having the same radius of 11.9 km with $\Delta R = 1.0, 0.5, 0.2$, and 0.1 km, respectively.
5. An analysis using all data listed in the first six rows in Table II from LIGO/VIRGO, Chandra+XMM-Newton, and NICER as a representation of the best data available. The resulting PDFs are used as references in studying the effects of improving the accuracy of measuring the radii of the four millisecond pulsars (MSPs) listed in the last four rows of Table II. Their masses are well-determined but their radii are only roughly known. We use $\Delta R = 1.0, 0.5, 0.2$, and 0.1 km, respectively, for all four MSPs.

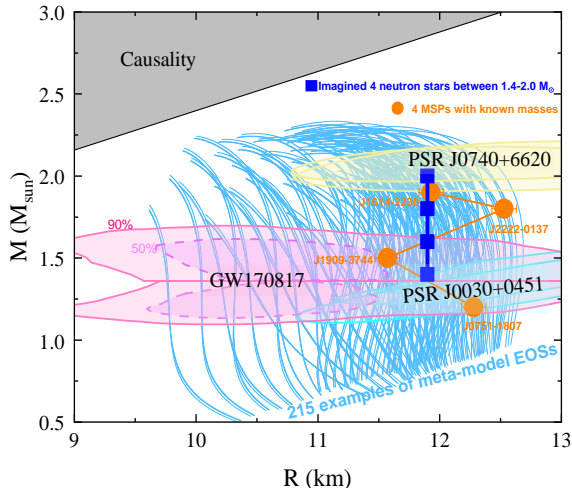


FIG. 1: (color online) Mass-radius sequences from using 215 examples of meta-model EOSs in comparison with the actual data from observations listed in Table II as well as some imagined NSs for the analyses in this work.

The real and imagined data used in the analyses listed above are illustrated in Fig. 1 on the background of mass-radius sequences predicted by 215 examples of meta-model EOSs with parameters covering their prior ranges listed in Table I.

III. RESULTS AND DISCUSSIONS

A. At the ultimate precision limit $\Delta R = 0$ of radius measurement: direct inversion by brute force of NS radii in the 3-dimensional parameter space of high-density nuclear symmetry energy

To help understand the results of statistical inference of EOS parameters from NS observations, we first examine constant surfaces of NS radii in the 3-dimensional (3D) parameter space $L - K_{\text{sym}} - J_{\text{sym}}$ of high-density nuclear symmetry energy. It has been shown earlier that NS inverse structure problems can be solved numerically by brute force [29–31, 71] by using the same meta-model EOS discussed above. Because of visualization limitations, for this work, we show in the left box of Fig. 2 the surfaces of $R_{1.4} = 11, 12,$ and 13 km in the $L - K_{\text{sym}} - J_{\text{sym}}$ space by fixing the relatively well-constrained saturation parameters at their currently known most probable values, i.e., $E_0(\rho_0) = -15.9$ MeV, $K_0 = 240$ MeV and $E_{\text{sym}}(\rho_0) = 31.7$ MeV. The skewness J_0 of SNM is set to -180 MeV based on earlier Bayesian analyses [32, 33], and it is known to have little influence on the radii of NSs [29] as we shall discuss in more detail. These constant-radius surfaces correspond to $\Delta R = 0$,

thus the ultimate limit of precise radius measurements. Examining the results shown in Fig. 2, we notice the following points most relevant for our understanding of the Bayesian results:

1. All three constant-radius surfaces for $R_{1.4}$ run through the whole range of J_{sym} considered, indicating that precise radius measurements of canonical NSs do not provide strong constraints on this parameter characterizing $E_{\text{sym}}(\rho)$ above about $3\rho_0$.
2. With a large radius, e.g., $R_{1.4} = 13$ km, both L and K_{sym} are at the large-positive corner of the $L - K_{\text{sym}}$ plane. The surface is rather vertical, indicating that its projection onto the $L - K_{\text{sym}}$ plane covers only a small range in the K_{sym} direction, and there is an approximately linear anti-correlation between L and K_{sym} . On the other hand, with a smaller radius, e.g., $R_{1.4} = 11$ km, L can be in its whole prior range from 30 to 90 MeV and K_{sym} covers a big range from about 0 to -400 MeV as the surface becomes more inclined in the negative K_{sym} direction. Moreover, the correlation between L and K_{sym} becomes more complicated. Furthermore, with the same separation of 1 km in radius, the separation in the 3D EOS parameter space between $R_{1.4} = 13$ km and 12 km is much larger than that between $R_{1.4} = 11$ km and 12 km, indicating a strong non-linear correspondence between $R_{1.4}$ and the EOS parameters especially the K_{sym} .
3. Based on the above observations, one can expect that in Bayesian analyses using NS radius data as the precision ΔR decreases from about 1 km to 0.1 km gradually, the peaks of the PDFs of L and K_{sym} will shift towards their lower boundaries. While the EOS parameters are generated uniformly in their prior ranges in each step of the MCMC process, with observational data of $R_{1.4} = 12$ km for example, there are many more combinations of EOS parameters on the right (lower R) than left (higher R) side to produce $R_{1.4}$ values within $12 \pm \Delta R$ km.
4. As the precision ΔR reaches its ultimate limit of zero, the Bayesian analyses should reveal the constant-radius surface. Every point on the surface represents a unique EOS. Namely, there are an infinite number of nuclear EOSs given a precise radius measurement. All the latter itself can constrain is the correlations among the EOS parameters. In the examples studied here, it is the correlations among $L - K_{\text{sym}} - J_{\text{sym}}$. Moreover, more precise radius measurements are expected to strengthen the correlations revealed. Furthermore, as indicated in earlier studies [29–31, 71], additional observables and/or physics filters/conditions may help break some of the correlations and thus narrow down the uncertainties of the EOS parameters.
5. Shown in the right box of Fig. 2 are the constant-radius surfaces of $R_{2.0} = 11$ km and 12 km, respec-

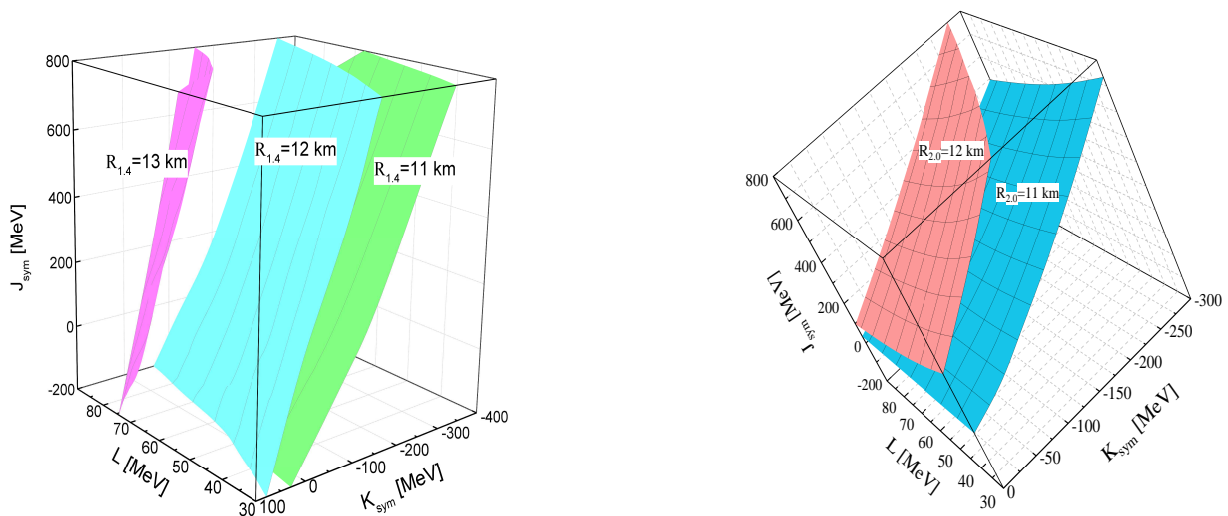


FIG. 2: (color online) Constant surfaces of NS radii in the 3-dimensional parameter space $L - K_{\text{sym}} - J_{\text{sym}}$ of high-density nuclear symmetry energy for $R_{1.4}$ (left) and $R_{2.0}$ (Right) with $E_0(\rho_0) = -15.9$ MeV, $K_0 = 240$ MeV, $E_{\text{sym}}(\rho_0) = 31.7$ MeV and $J_0 = -180$ MeV, respectively.

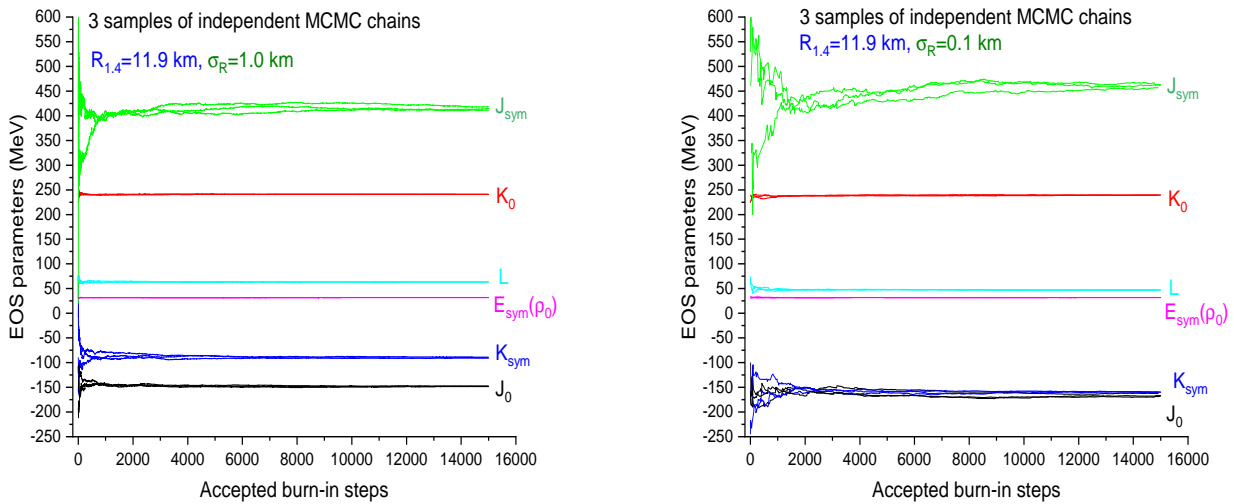


FIG. 3: (color online) Examples of the tracing plots (running averages) of the 6 EOS parameters during the burn-in stage of the MCMC process from 3 independent runners.

tively. Since to obtain the mass $2.0M_{\odot}$, a rather stiff high-density SNM EOS is required. In this example, using the same $J_0 = -180$ MeV as for the calculation of constant surfaces of $R_{1.4}$, it is impossible to obtain a large radius of $R_{2.0} = 13$ km. The radius $R_{2.0}$ of $2.0 M_{\odot}$ NS indeed depends more on the high-density symmetry energy parameter J_{sym} . The surface $R_{2.0} = 12$ km requires significantly larger J_{sym} values compared to the $R_{2.0} = 11$ km surface. Comparing the 11 km and 12 km sur-

faces for $R_{1.4}$ and $R_{2.0}$, respectively, it is seen that changing $R_{2.0}$ by 1 km does not require as much change in K_{sym} as for $R_{1.4}$. For both values of $R_{2.0}$ considered, the whole prior range of L is acceptable. Thus, one expects the high-precision measurements of $R_{2.0}$ may put more constraints on J_{sym} but less on K_{sym} and L compared to the measurements of $R_{1.4}$.

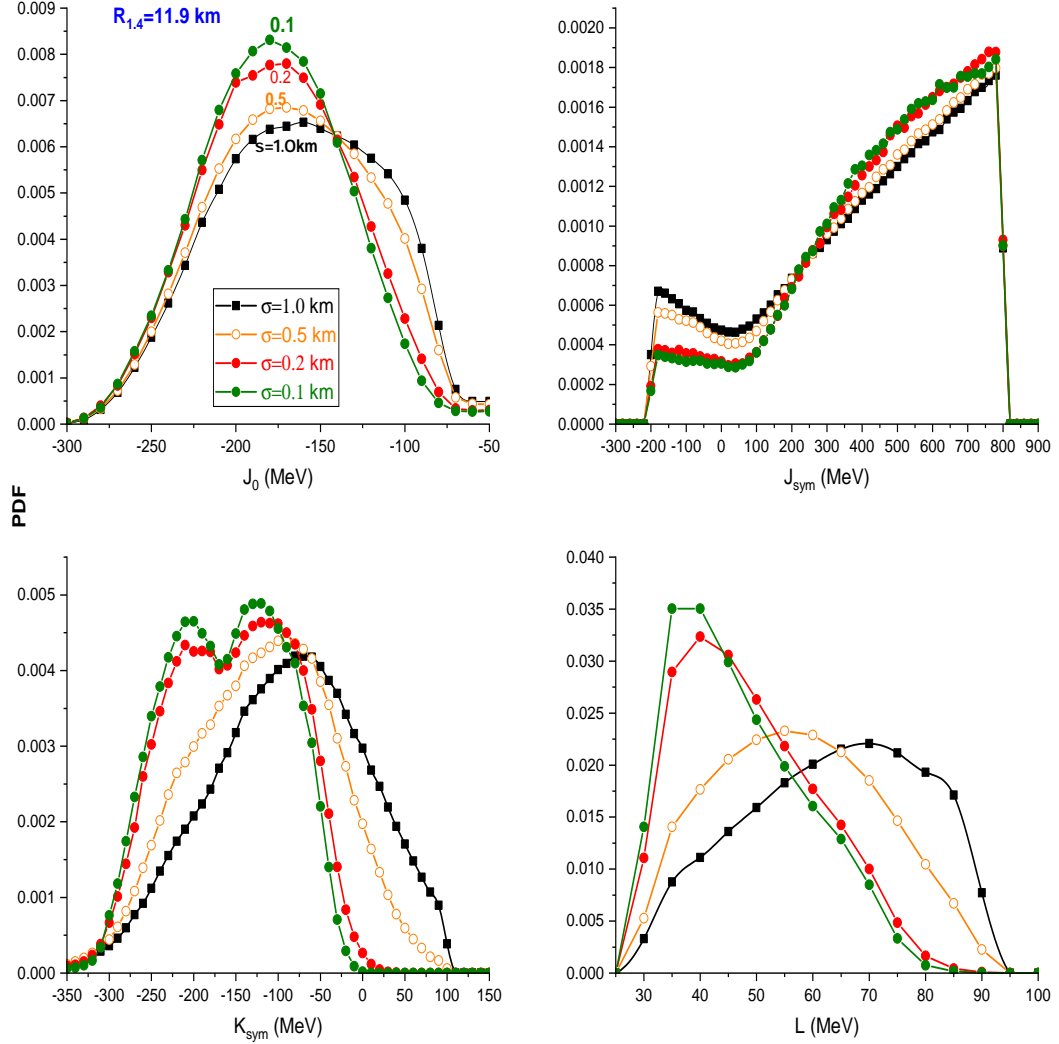


FIG. 4: (color online) Posterior PDFs of EOS parameters with $R_{1.4} = 11.9$ km and a precision of $\Delta R = 1.0, 0.5, 0.2$, and 0.1 km, respectively.

B. The burn-in steps of the MCMC process

In our Bayesian analyses, the Metropolis-Hastings algorithm is utilized in the MCMC process to generate posterior PDFs for the EOS model parameters. These PDFs not only encompass the individual parameters but also enable the calculation of two-parameter correlations by integrating all other parameters via the marginal estimation approach. During the initial phase, known as the burn-in period, samples are discarded to ensure that the posterior PDFs represent equilibrium distributions, as recommended by Trotta (2017)[72]. Shown in Fig. 3 are examples of the running averages of the six EOS pa-

rameters during the burn-in stage of the MCMC process from 3 independent runners. As examples, here we used only $R_{1.4} = 11.9$ km with $\Delta R = 1.0$ km (left) and 0.1 km (right), respectively. It is seen that they quickly converge (indicating the constraining power of the observables and filters used), especially in the case of $\Delta R = 1.0$ km. We also notice that K_0 and $E_{\text{sym}}(\rho_0)$ do not change much as they have little influence on the radii of NSs compared to the supersaturation density parameters L , K_{sym} , J_{sym} and J_0 . In the following analyses, we shall thus focus on the latter four parameters. It is interesting to also note that the stabilized mean values of L and K_{sym} decrease appreciably while the mean of J_{sym} increases when the

ΔR changes from 1.0 km to 0.1 km. The other three parameters show no obvious change. These indications will be studied in detail by examining their posterior PDFs.

It is seen that 15,000 burn-in steps are more than enough for all runners to reach the equilibrium stage. All results presented in the following are obtained from using at least 600,000 subsequent steps by each runner for calculating the posterior PDFs. Since gradually fewer steps are accepted in the MCMC process with higher precision ΔR , 24 to 48 runners are used with different radius precision. We have checked that our results are stable by adding or reducing 8 runners in accumulating the posterior EOS data.

TABLE III: Most probable values and their corresponding 68% credible intervals of the four EOS parameters inferred from Bayesian analyses using $R_{1.4}=11.9$ km with precision ΔR from 1.0 to 0.1 km.

Parameters (MeV)	$\Delta R=1.0$	$\Delta R=0.5$	$\Delta R=0.2$	$\Delta R=0.1$
J_0 :	-160^{+60}_{-50}	-170^{+60}_{-50}	-170^{+40}_{-50}	-180^{+50}_{-40}
J_{sym} :	780^{+0}_{-480}	780^{+0}_{460}	780^{+0}_{-420}	780^{+0}_{-420}
K_{sym} :	-70^{+80}_{-100}	-100^{+70}_{-100}	-120^{+50}_{-100}	-130^{+50}_{-100}
L :	70^{+5}_{-40}	55^{+15}_{-25}	40^{+15}_{-10}	35^{+20}_{-5}

TABLE IV: Means and standard deviations of the four EOS parameters (MeV) inferred from Bayesian analyses using $R_{1.4}=11.9$ km with precision ΔR from 1.0 to 0.1 km.

Pars.	$\Delta R=1.0$	$\Delta R=0.5$	$\Delta R=0.2$	$\Delta R=0.1$
J_0 :	-149 ± 71	-149 ± 71	-161 ± 71	-164 ± 70
J_{sym} :	417 ± 277	431 ± 269	461 ± 248	463 ± 243
K_{sym} :	-89 ± 91	-119 ± 84	-154 ± 72	-162 ± 69
L :	63 ± 16	57 ± 15	49 ± 12	47 ± 12

C. What can we learn from the data $R_{1.4} = 11.9$ km with precision $\Delta R = 1.0, 0.5, 0.2$, and 0.1 km?

Shown in Fig. 4 are the posterior PDFs of J_0 , J_{sym} , K_{sym} , and L , using the radius data of $R_{1.4} = 11.9$ km with a precision of $\Delta R = 1.0, 0.5, 0.2$, and 0.1 km, respectively. The PDFs of K_0 and $E_{\text{sym}}(\rho_0)$ are not shown as they are not sensitive to the variation of ΔR as mentioned earlier. Since most of the PDFs are asymmetric, both the most probable values (MPVs) and means of the EOS parameters are informative. Listed in Table III are the MPVs and the highest posterior density (HPD) 68% confidence intervals calculated using the approach given in Ref. [73]. The means and standard deviations of the four parameters are listed in Table IV. We notice that in our analyses we used a bin size of 5 MeV for L , but 10 MeV is used for the other three EOS parameters shown here. Several interesting observations can be made:

1. Both the MPVs and means of J_0 , K_{sym} and L gradually decrease, especially for the last two, as ΔR decreases. They become approximately stabilized within the bin sizes used after $\Delta R \leq 0.2$ km. This is consistent with our expectations based on the results shown in Fig. 2. It means that the currently available MPVs and means of these parameters, especially K_{sym} and L , from various Bayesian analyses by many groups in the community of the available data with NS radii measured mostly with $\Delta R \geq 1.0$ km are unreliable. High precision measurements with $\Delta R \leq 0.2$ km will be necessary to extract stable MPVs and means of J_0 , J_{sym} , K_{sym} and L .
2. On the other hand, the mean of skewness J_{sym} of symmetry energy becomes larger as the precision of measuring the radius improves. This is mainly due to its anti-correlation with both J_0 and K_{sym} as we shall discuss. It is known from previous Bayesian analyses [32, 34] of NS radius data, the radius $R_{1.4}$ does not effectively constrain J_{sym} as indicated by the peak of its PDF at its upper boundary. The sharp drop there is due to the cut-off from its prior PDF used. Nevertheless, it is interesting to see that as ΔR decreases, because the pairwise anti-correlations of $J_{\text{sym}} - J_0$ and $J_{\text{sym}} - K_{\text{sym}}$ become stronger, the mean value of J_{sym} increases to counterbalance the decreases of J_0 and K_{sym} .
3. Very interestingly, a distinguished two-peak structure is revealed in the PDF of K_{sym} when the precision of NS radius measurement is better than about 0.2 km. Generally speaking, it is not surprising that fine structures can be seen when the probes used have better resolutions. As we shall discuss next, the two-peak structure of PDF(K_{sym}) is completely due to the strong anti-correlations of $K_{\text{sym}} - J_{\text{sym}}$ and $K_{\text{sym}} - L$ that are only visible when the precision ΔR is better than about 0.2 km.

Shown in Fig. 5 are the posterior pairwise correlation functions among the four high-density EOS parameters using $R_{1.4}=11.9$ km with a precision of $\Delta R=1.0$ km (upper panels) and 0.1 km (middle panels), respectively. The bottom panels compare their 68% HPD confidence boundaries to be more quantitative. In parameterizing the SNM EOS $E_0(\rho)$ and symmetry energy $E_{\text{sym}}(\rho)$, any two adjacent parameters are mathematically expected to be anti-correlated. While the correlations among parameters of $E_0(\rho)$ and those of $E_{\text{sym}}(\rho)$ are mostly due to the physical requirements, e.g., β -equilibrium, the final EOS has to be stiff enough to support NSs at least as massive as $1.97M_\odot$ and causality condition. The total pressure has contributions from both SNM EOS and nuclear symmetry energy. For instance, the contributions from J_0 and J_{sym} are complementary, their PDFs inferred from NS data are thus expected to be anti-correlated, albeit weakly, especially for canonical NSs.

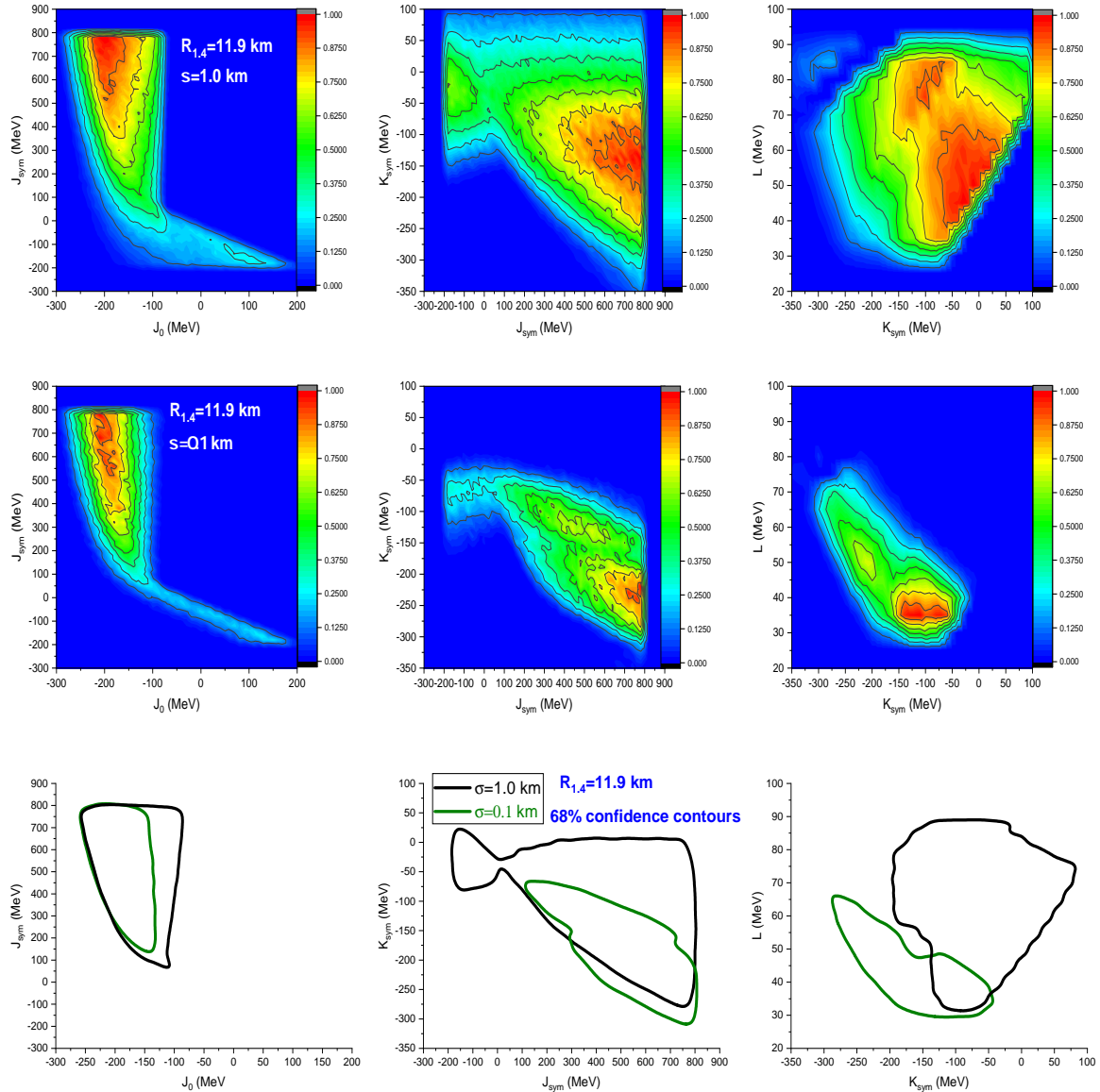


FIG. 5: (color online) Posterior correlation functions among the four high-density EOS parameters using $R_{1.4}=11.9$ km and a precision of $\Delta R=1.0$ km (upper panels) and 0.1 km (middle panels), respectively. The bottom panels compare their 68% confidence boundaries.

Indeed, as shown in Fig. 5, $J_{\text{sym}} - J_0$ and $J_{\text{sym}} - K_{\text{sym}}$ are clearly anti-correlated. Most interestingly, it is seen that the strengths of all correlations depend strongly on the precision ΔR . In particular, comparing the correlations obtained with $\Delta R = 1.0$ km and 0.1 km, the strong anti-correlations of $K_{\text{sym}} - J_{\text{sym}}$ around ($K_{\text{sym}} = -250$ MeV, $J_{\text{sym}} = 800$ MeV) and $K_{\text{sym}} - L$ around ($K_{\text{sym}} = -120$ MeV, $L = 35$ MeV), especially the latter, is only clearly visible with $\Delta R = 0.1$ km. Thus, in the case of $\Delta R = 0.1$ km, corresponding to the peaks of PDFs around $J_{\text{sym}} = 800$ MeV and $L = 35$ MeV, there are two peaks in the PDF(K_{sym}) around $K_{\text{sym}} = -250$ MeV and -120 MeV, respectively, as shown in Fig. 4. This

clearly shows the resolving power of high-precision NS radius measurements. To be more quantitative, in the bottom panels we have compared the 68% HPD boundaries of the correlations obtained with $\Delta R = 1.0$ km and 0.1 km, respectively. It is seen that the correlations are more focused, especially for $K_{\text{sym}} - J_{\text{sym}}$ and $K_{\text{sym}} - L$ as K_{sym} is the most important parameter determining $R_{1.4}$ as mentioned earlier, with the high-precision measurement of $\Delta R = 0.1$ km.

To further understand the results presented above, shown in Fig. 6 are the posterior PDF of $R_{1.4}$ from the Bayesian analysis using the NS radius data of $R_{1.4}=11.9$ km with the precision $\Delta R=1.0$ km and $\Delta R=0.1$ km as

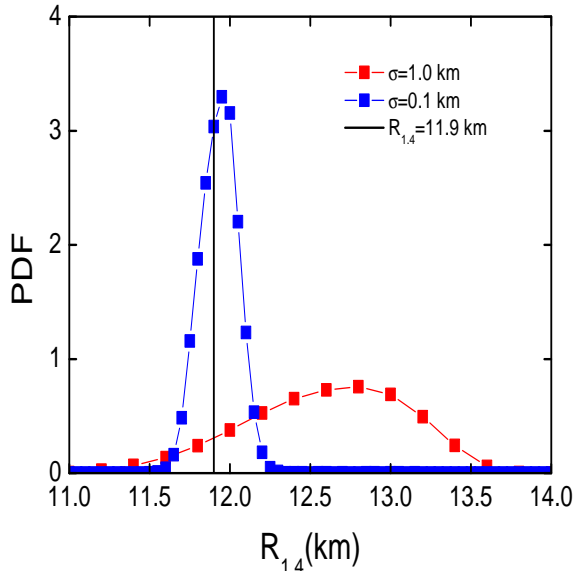


FIG. 6: (color online) Posterior PDFs of $R_{1.4}$ obtained with the input data $R_{1.4} = 11.9$ km and a precision of $\Delta R = 1.0$ km and 0.1 km, respectively.

indicated. As listed in Table IV, when $R_{1.4}=11.9$ km with different precision from 1.0 to 0.1 km are used as input data in the Bayesian analysis, the necessary NS EOS effectively becomes softer as shown by the decreasing mean values of J_0 , L , and K_{sym} . This implies that the posterior NS radius predicted is smaller using the precision $\Delta R=0.1$ km than that using $\Delta R=1.0$ km. Several factors can make this happen. As we mentioned earlier, while the EOS parameters are initialized randomly and uniformly within their prior range, the predicted NS radii are not uniform or symmetric about some central values as the underlying physics is highly nonlinear. Also, although the likelihood function of observable R is symmetric with respect to the input mean value of $R_{1.4}$ data, the physics requirements/filters in the MCMC process break the symmetry. Consequently, the accepted predictions of $R_{1.4}$ during the MCMC process are not necessarily symmetric about the mean value of $R_{1.4}$ data. This is consistent with the results of direct inversions shown in Fig. 2 and the associated expectations discussed in Section III A. Indeed, as clearly indicated by the posterior PDF of the accepted $R_{1.4}$ in Fig. 6, finally a larger (smaller) posterior radius $R_{1.4}$ is preferred when $\Delta R=1.0$ (0.1) km is used with the same input $R_{1.4}=11.9$ km in the calculations. Interestingly, as the precision improves, the MPV of the posterior $R_{1.4}$ moves towards its input value of 11.9 km (dark vertical line). Even with $\Delta R = 0.1$ km, however, it is still about 0.1 km away. This finding demonstrates once again the importance of high-precision

radius measurements.

D. What more can we learn from comparing the results using a radius of $R_{1.4} = 11.8, 11.9$ and 12.0 km all with a precision of $\Delta R = 0.1$ km?

In the studies so far, we have adopted the mean radius $R_{1.4} = 11.9$ km based on the analysis of GW17087 by the LIGO/VIRGO Collaboration [70]. It is necessary to study if the two-peak structure of $\text{PDF}(K_{\text{sym}})$ persists if R itself is changed by about the same amount as ΔR . We thus compare in Fig. 7 the PDFs of the four key EOS parameters obtained by using $R_{1.4} = 11.8, 11.9$ and 12.0 km all with a precision $\Delta R = 0.1$ km. The mean values and the standard deviations of the four EOS parameters are also shown in the plot. Firstly, it is seen that the two-peak structure of $\text{PDF}(K_{\text{sym}})$ persists in all three cases. Secondly, as the radius increases from 11.8 km to 12.0 km, the mean value of J_0 increases by about 4%, that of J_{sym} has little change, while those of K_{sym} and L increase by about 15% and 2%, respectively, to make the EOS more stiff as required by the slightly larger radius. Again, it indicates that K_{sym} is most important for determining the radii of NSs.

With the increasing radius $R_{1.4}$, the first peak of $\text{PDF}(K_{\text{sym}})$ around $K_{\text{sym}} = -125$ MeV gradually shifts towards larger K_{sym} values and the peak of $\text{PDF}(L)$ shifts towards higher L values as the resulting symmetry energy has to be stiff enough to make the radius larger. The underlying physics causing the two peaks are still due to the $K_{\text{sym}} - J_{\text{sym}}$ and $K_{\text{sym}} - L$ correlations as shown in Fig. 8. Consistent with the PDFs shown in Fig. 7, there are small slight shifts in the locations of highest strength in the correlations. Comparing the two sets of correlations with $R_{1.4} = 11.8$ km and 12.0 km shown in Fig. 8, we also notice that with the large radius, the $K_{\text{sym}} - J_{\text{sym}}$ correlation around $K_{\text{sym}} = -220$ MeV and $J_{\text{sym}} = 800$ MeV becomes weaker indicated by the more broad spread in the area while the $K_{\text{sym}} - L$ correlation becomes stronger around $K_{\text{sym}} = -100$ MeV and $L = 40$ MeV. This leads to the slightly different heights of the two peaks in $\text{PDF}(K_{\text{sym}})$ shown in Fig. 7.

E. What more can we learn from the radius $R_{2.0} = 11.9$ km of a massive NS of mass $2.0M_{\odot}$ with a varying precision of $\Delta R = 1.0, 0.5, 0.2$, and 0.1 km?

Compared to what we have learned from the above analyses using the radii of canonical NSs, what possibly more physics can we learn from studying the radii of more massive NSs? To answer this question, we performed comprehensive analyses using $R_{2.0} = 11.9$ km with different precision. Shown in Figs. 9 and 10 are the PDFs and pairwise correlations of the four key EOS parameters. Their MPVs with 68% HPD boundaries, means and standard deviations are listed in Tables V

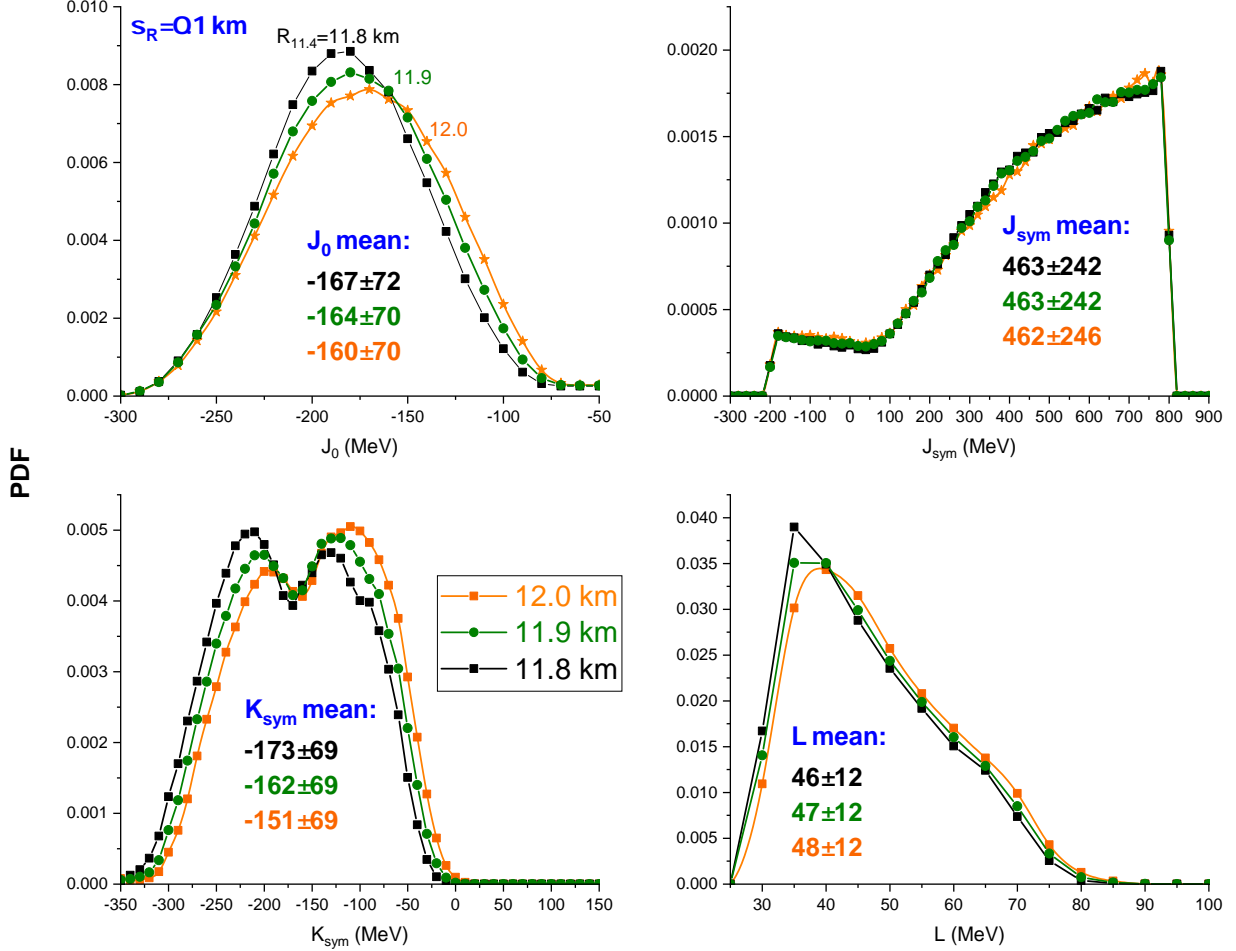


FIG. 7: (color online) Posterior PDFs of the four EOS parameters with $R_{1.4} = 11.8, 11.9$ and 12.0 km all with a precision of $\Delta R = 0.1$ km, respectively.

and VI, respectively. It is interesting to note particularly the following points:

1. The effects of precision ΔR in measuring $R_{2.0}$ on the PDFs and correlation functions of K_{sym} and L are not as strong as in the case of measuring $R_{1.4}$. This is not surprising as $R_{2.0}$ depends more on the EOS at higher densities than $R_{1.4}$. Indeed, it is seen that the PDF of J_{sym} near its upper limit is more affected by the ΔR , indicating the potential of better constraining this very poorly known parameter characterizing the symmetry energy at densities around $(3 - 4)\rho_0$. Comparing the PDF of J_{sym} in this case to that with $R_{1.4} = 11.9$ km, its peak near the upper limit of J_{sym} is significantly lower. Consequently, the mean value of J_{sym} is reduced from 463 ± 243 (with $R_{1.4} = 11.9$ km) to 387 ± 279 (with $R_{2.0} = 11.9$ km) at $\Delta R = 0.1$ km

as listed in Tables IV and VI. One reason for this finding is that the required skewness J_0 of SNM is slightly higher to make the EOS stiff enough to support a $2.0M_{\odot}$ NS as also listed in Tables IV and VI. Since J_{sym} and J_0 are anti-correlated as shown in Fig. 10, the mean value of J_{sym} needs to be lower corresponding to a higher J_0 with $R_{2.0} = 11.9$ km. However, we notice that this effect is expected to be small as we already used the requirement that all EOSs have to be stiff enough to support NSs at least as massive as $1.97M_{\odot}$. Another possibly more important reason as we shall elaborate more next is the anti-correlations of K_{sym} with both J_{sym} and L . For a NS of mass $2.0M_{\odot}$ to have the same radius of 11.9 km as a $1.4M_{\odot}$ NS, the required mean value of K_{sym} is higher than that in the case of $R_{1.4} = 11.9$ km especially in the high-precision measurements. Thus, the anti-correlation between K_{sym} and J_{sym}

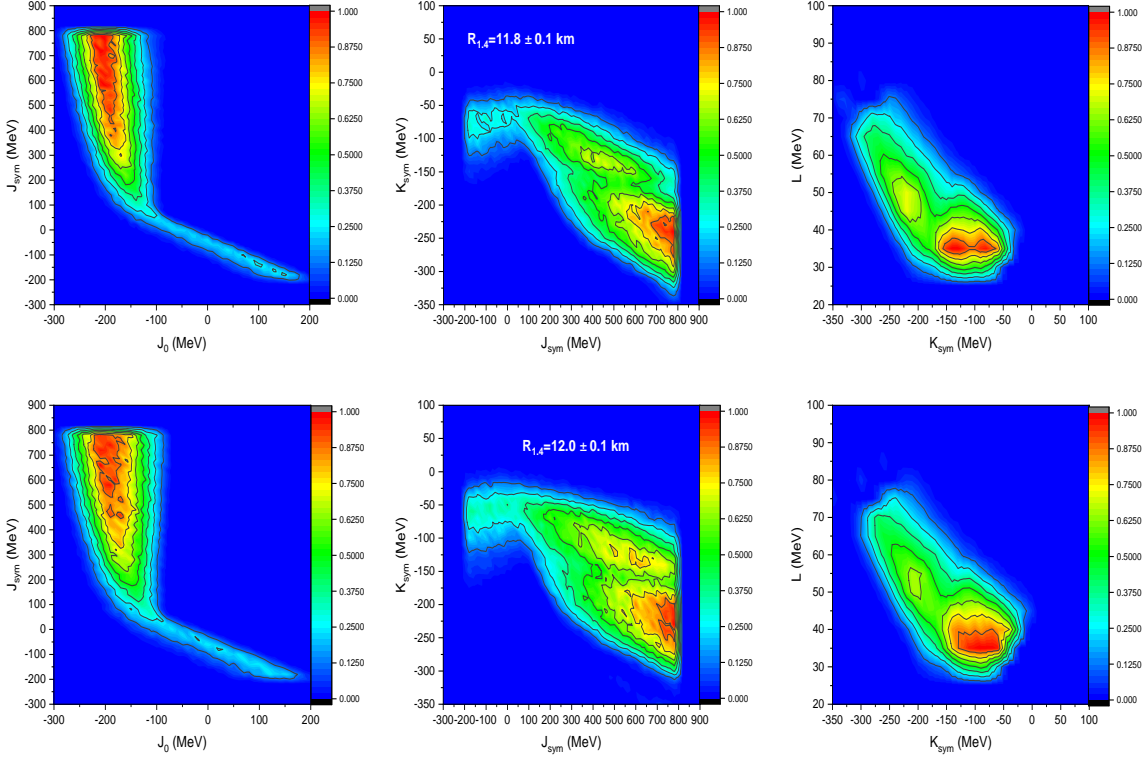


FIG. 8: (color online) Posterior correlation functions among the four high-density EOS parameters using $R_{1.4}=11.8$ km (upper panels) and 12.0 km (lower panels) and a precision of $\Delta R=0.1$ km, respectively.

also requires the latter to become smaller in the case of $R_{2.0} = 11.9$ km.

- There is no longer any two-peak structure in the PDF of K_{sym} with $R_{2.0} = 11.9$ km even at high precision. Its stabilized single peak around $K_{\text{sym}} \approx -100$ MeV with $\Delta R = 0.1$ or 0.2 km is the result of a competition between $K_{\text{sym}} - L$ and $K_{\text{sym}} - J_{\text{sym}}$ anti-correlations. As shown in Fig. 10, the $K_{\text{sym}} - L$ anti-correlation is the strongest around ($K_{\text{sym}} = -40$ MeV, $L = 50$ MeV) with $\Delta R = 0.1$ km, while the $K_{\text{sym}} - J_{\text{sym}}$ anti-correlation peaks around ($K_{\text{sym}} = -220$ MeV, $J_{\text{sym}} = 800$ MeV). Whether there exists two-peaks or a single peak in the PDF of K_{sym} and its location depend on both the strengths of the above two anti-correlations as well the mean values of J_{sym} and L . Besides the changes of the mean values of J_{sym} mentioned above, it is also seen in Tables IV and VI that the mean value of L changes from 47 ± 12 (with $R_{1.4} = 11.9$ km) to 62 ± 16 MeV (with $R_{2.0} = 11.9$ km) with $\Delta R = 0.1$ km. These changes of posterior mean values of the EOS parameters are also shown in Fig. 11. Since a larger L prefers a smaller K_{sym} while a reduced J_{sym} prefers a larger one both with $R_{2.0} = 11.9$ km, compared to the case with $R_{1.4} = 11.9$ km, their competition makes

the PDF(K_{sym}) to have a single peak around -100 MeV as observed instead of two peaks. It is seen from Figs. 10 and 5, the anti-correlation $K_{\text{sym}} - L$ is much weaker or more spread out with $R_{2.0} = 11.9$ km, as $R_{2.0}$ does not constrain tightly L which characterizes the symmetry energy below about $1.5\rho_0$. It is also seen that improving the precision of measuring $R_{2.0}$ from $\Delta R = 1.0$ km to 0.1 km has the strongest effect in narrowing down the $K_{\text{sym}}-J_{\text{sym}}$ correlation.

- Shown in Fig. 11 are comparisons of the mean and standard deviations of all six EOS parameters inferred from using the $R_{1.4}$ and $R_{2.0}$ data with ΔR from 1.0 to 0.1 km. It is seen that at poor precision, e.g., $\Delta R=1.0$ km, the results from using the $R_{1.4}$ and $R_{2.0}$ data are about the same. As one expects and demonstrated above, the differences gradually appear as the precision gets better especially using the $R_{1.4}$ data. Overall, only the symmetry parameters show appreciable changes with respect to their individual prior scales.
- It is seen in Fig. 11 that L and K_{sym} are lower while the J_{sym} is higher to obtain $R_{1.4} = 11.9$ km than $R_{2.0} = 11.9$ km at high precision. This has important implications on the density profiles of proton

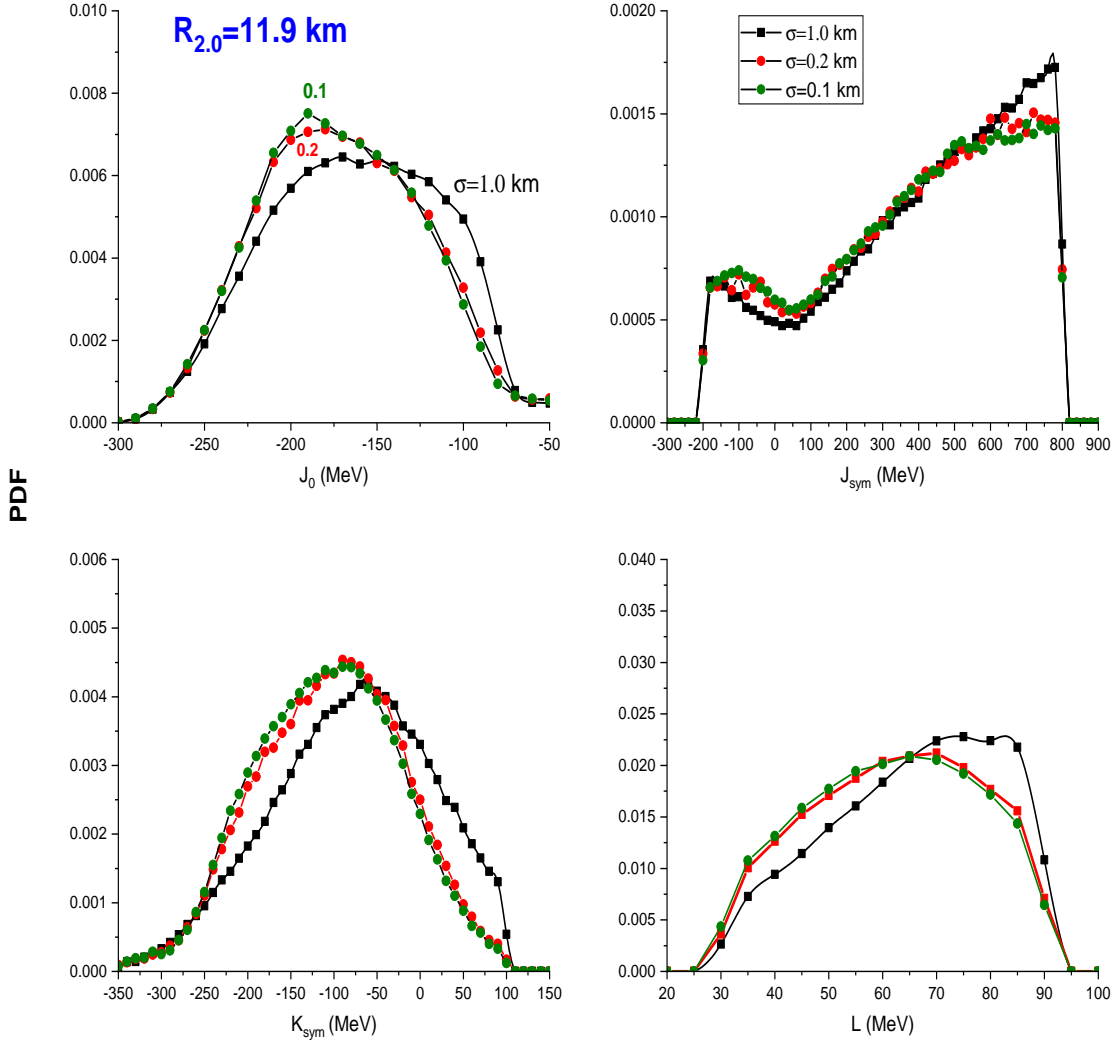


FIG. 9: (color online) Posterior PDFs of the four EOS parameters obtained with $R_{2.0} = 11.9$ km and a precision of $\Delta R = 1.0$ km, 0.5, 0.2 and 0.1 km, respectively.

fraction x_p (or isospin asymmetry $\delta = (1 - 2x_p)$) at β -equilibrium, and subsequently whether and where the fast cooling through the direct URCA process (requiring $x_p \geq 11\%$) [74, 75] can happen or not in the two NSs considered. Lower values of L and K_{sym} indicate that the symmetry energy at low-intermediate densities $(1 - 2)\rho_0$ is lower/softer, while a higher J_{sym} implies that the symmetry energy around $(3 - 4)\rho_0$ is higher/stiffer in a canonical NS with $R_{1.4} = 11.9$ km compared to a NS of mass $2.0M_\odot$ with the same radius. It is well known that to minimize the total energy of isospin asymmetric nuclear matter because of the $E_{\text{sym}}(\rho)\delta^2$

term in its EOS, wherever/whenever the symmetry energy is higher the isospin asymmetry δ there is lower. The resulting density profile $\delta(\rho)$ at β -equilibrium exhibits the so-called isospin fractionation phenomenon ($E_{\text{sym}}(\rho_1)\delta_1 \approx E_{\text{sym}}(\rho_2)\delta_2$) for two regions of density ρ_1 and ρ_2 in β -equilibrium [76, 77]), see, e.g., Ref. [24] for a review. The results shown in Fig. 11 obtained under the assumption that $R_{2.0} = R_{1.4} = 11.9$ km imply that the massive NS of $2.0M_\odot$ is more neutron-rich at high densities $((3 - 4)\rho_0)$ but neutron-poor at low-intermediate densities $((1 - 2)\rho_0)$ compared to a canonical NS. As indicated, however, this informa-

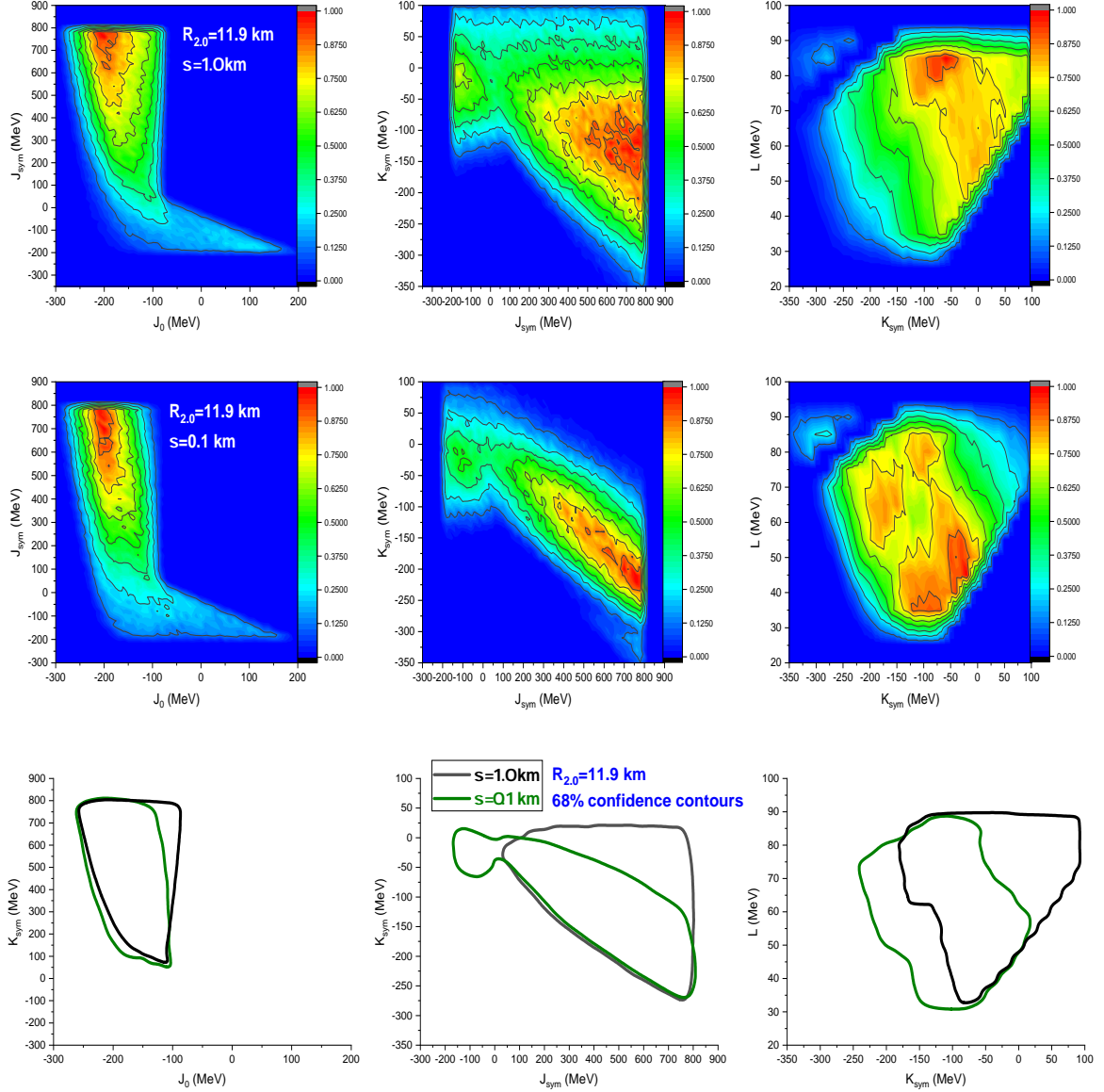


FIG. 10: (color online) Posterior correlation functions among the four high-density EOS parameters using $R_{2.0}=11.9$ km and a precision of $\Delta R=1.0$ km (upper panels) and 0.1 km (middle panels), respectively. The bottom panels compare their 68% confidence boundaries.

tion can only be inferred from high-precision radius measurements. In this sense, the latter will help better understand the cooling mechanisms of protoneutron stars and their NS mass dependence [78].

F. What more can we learn from assuming $R_{1.4} = R_{1.6} = R_{1.8} = R_{2.0} = 11.9$ km with varying precision?

With the current precision of about $\Delta R \geq 1.0$ km in measuring the radii of NSs, most of the existing data indicate empirically $R_{1.4} \approx R_{1.6} \approx R_{1.8} \approx R_{2.0} \approx 11.9$ km, see e.g., Ref. [11] for a recent summary. As we have shown above, with $\Delta R = 1.0$ km, one can not distinguish the PDFs and correlations of EOS parameters inferred from $R_{1.4} = 11.9$ or $R_{2.0} = 11.9$ km. However, as the precision improves, their differences are clearly

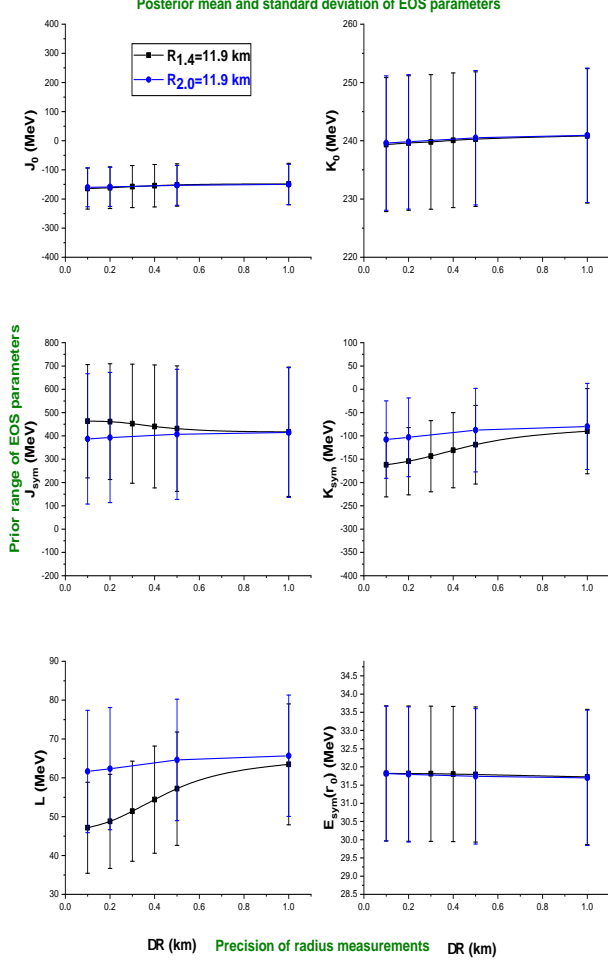


FIG. 11: (color online) Comparisons of the mean and standard deviations of all six EOS parameters inferred from using the $R_{1.4}$ and $R_{2.0}$ data with a varying precision from 1.0 to 0.1 km.

visible. In particular, at high precision, the PDF(K_{sym}) has a distinctive two-peak structure for $1.4M_{\odot}$ but not for $2.0M_{\odot}$ NS. While we have not studied at what NS mass this two-peak feature will start disappearing because of the extremely expensive computing costs, we present here results of one calculation using combined data (the radius likelihood functions of the four NSs of different masses are multiplied together) assuming $R_{1.4} = R_{1.6} = R_{1.8} = R_{2.0} = 11.9$ km. One generally expects the NS central density to increase with its mass. Thus, it is interesting to know which EOS parameters are required to change most when the four NSs of different masses are forced to have the same radius.

Shown in Fig. 12 are the posterior PDFs of the four parameters characterizing the density dependencies of nuclear symmetry energy. It is seen that the PDFs of L , K_{sym} , and J_{sym} all show significant dependencies on ΔR .

TABLE V: Most probable values and their corresponding 68% credible intervals of the four EOS parameters inferred from Bayesian analyses using $R_{2.0}=11.9$ km with precision ΔR from 1.0 to 0.1 km.

Parameters (MeV)	$\Delta R=1.0$	$\Delta R=0.5$	$\Delta R=0.2$	$\Delta R=0.1$
J_0 :	-170^{+70}_{-40}	-170^{+60}_{-50}	-180^{+60}_{-40}	-190^{+70}_{-30}
J_{sym} :	780^{+0}_{-500}	780^{+0}_{460}	780^{+0}_{-520}	780^{+0}_{-520}
K_{sym} :	-60^{+90}_{-100}	-70^{+80}_{-100}	-90^{+70}_{-100}	-90^{+70}_{-100}
L :	75^{+0}_{-40}	70^{+5}_{-40}	70^{+0}_{-40}	65^{+5}_{-35}

TABLE VI: Means and variances of the four EOS parameters (MeV) inferred from Bayesian analyses using $R_{2.0}=11.9$ km with precision ΔR from 1.0 to 0.1 km.

Pars.	$\Delta R=1.0$	$\Delta R=0.5$	$\Delta R=0.2$	$\Delta R=0.1$
J_0 :	-150 ± 69	-153 ± 68	-158 ± 67	-160 ± 67
J_{sym} :	414 ± 278	407 ± 279	393 ± 279	387 ± 279
K_{sym} :	-80 ± 92	-88 ± 90	-103 ± 84	-108 ± 83
L :	66 ± 16	65 ± 16	62 ± 16	62 ± 16

Most features observed in analyzing only the $R_{1.4} = 11.9$ km data are again apparent. For the PDF of $E_{\text{sym}}(\rho_0)$, while the fluctuations become more obvious with higher precision as one expects, overall the high-precision NS radius measurement does not provide any new information about $E_{\text{sym}}(\rho_0)$ compared to our prior knowledge. The two-peak structure of the PDF(K_{sym}) remains and the PDF(J_{sym}) appears to show stronger sensitivity to ΔR compared to the results from studying separately the $R_{1.4} = 11.9$ km and $R_{2.0} = 11.9$ km cases earlier. This observation is understandable. As noticed before, the peak of PDF(K_{sym}) around $K_{\text{sym}} \approx -220$ MeV is due to the anti-correlation between K_{sym} and J_{sym} . While its second peak around $K_{\text{sym}} \approx -120$ MeV is due to the anti-correlation between K_{sym} and L that is most visible for canonical NSs with high precision. Thus, the combined analyses assuming $R_{1.4} = R_{1.6} = R_{1.8} = R_{2.0} = 11.9$ km at high precision maintain both peaks in the PDF(K_{sym}). Moreover, with more massive NSs involved in the analyses, the J_{sym} plays a more significant role. Consequently, its PDF(J_{sym}) appears more sensitive to ΔR .

Shown in Fig. 13 are the posterior PDFs of the skewness parameter J_0 of SNM EOS (left) and the maximum mass M_{TOV} (right) assuming $R_{1.4} = R_{1.6} = R_{1.8} = R_{2.0} = 11.9$ km with varying precision. The PDF(J_0) is consistent with that observed earlier from analyzing the $R_{1.4} = 11.9$ km and $R_{2.0} = 11.9$ km cases. The maximum mass M_{TOV} of NSs on the mass-radius sequence given a NS EOS is determined mostly by the J_0 while the J_{sym} plays a less important role, see e.g., Refs. [10, 79] for reviews. Because of the anti-correlation between J_{sym} and J_0 as shown earlier, the PDF of M_{TOV} peaked around $M_{\text{TOV}} \approx 2.25 M_{\odot}$ does not show much dependence on the precision ΔR . This is not surprising as the latter affects directly only the radii of NSs. Its secondary effect

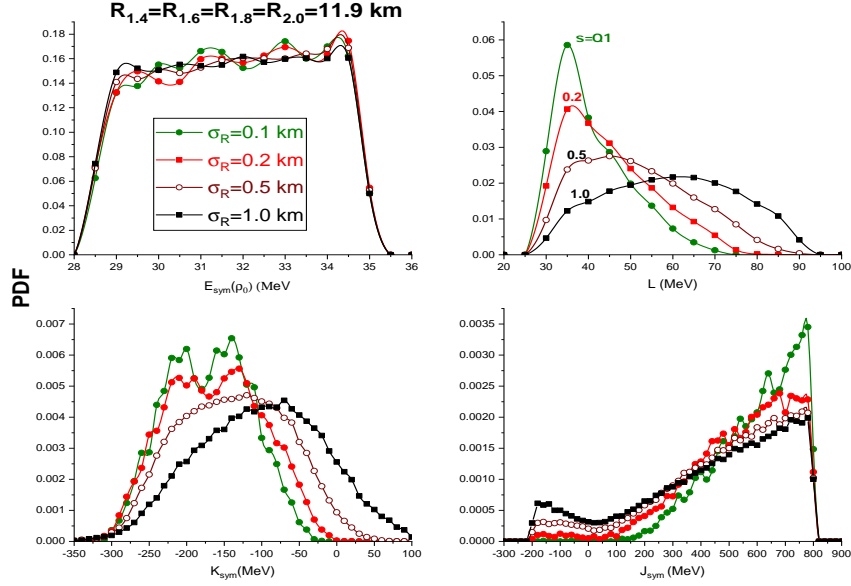


FIG. 12: (color online) Posterior PDFs of the four parameters characterizing the density dependence of nuclear symmetry energy assuming $R_{1.4} = R_{1.6} = R_{1.8} = R_{2.0} = 11.9$ with a varying precision indicated.

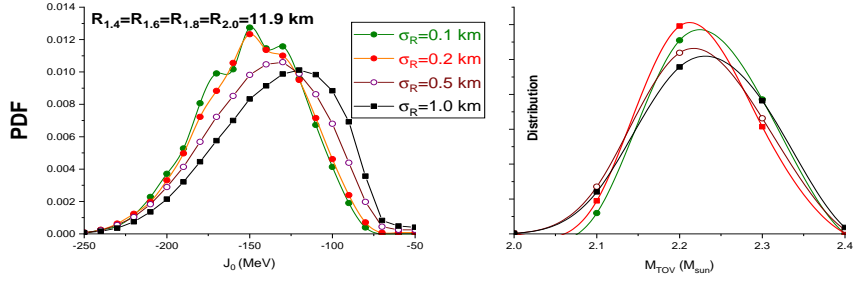


FIG. 13: (color online) Posterior PDFs of the skewness parameter J_0 of SNM EOS (left) and the maximum mass M_{TOV} (right) assuming $R_{1.4} = R_{1.6} = R_{1.8} = R_{2.0} = 11.9$ km with a varying precision indicated.

on M_{TOV} is thus small. It is interesting to point out here that the $\text{PDF}(M_{\text{TOV}})$ obtained here is in perfect agreement with the very recent finding of $M_{\text{TOV}} = 2.25^{+0.08}_{-0.07} M_{\odot}$ from a comprehensive analysis using two approaches: (1) modeling the mass function of 136 NSs with a sharp cut-off at $2.28 M_{\odot}$, and (2) Bayesian inference of the EOS from the available combined multi-messenger data of NSs considering constraints from the chiral effective field theory at low densities and the perturbative QCD at very high densities [80].

G. What more can we learn from the radii of the four MSPs that are about 1.0 km apart with $\Delta R = 1.0, 0.5, 0.2$ and 0.1 km, with respect to what we knew from analyzing the radii of GW170817, PSR J0030+0451 and PSR J0740+6620?

In the new era of multimessenger astronomy, combined data of multiple observables obtained using different tools over possibly multiple sources are often used in Bayesian analyses. Based on what we have learned so far from the above analyses, different precision of different messengers from NSs of different masses may be a concern to be taken care of. Nevertheless, we emphasize that such practice may be important for studying the local derivative dM/dR of the mass-radius sequence. Such information is important for investigating the possible existence of twin stars having approximately the

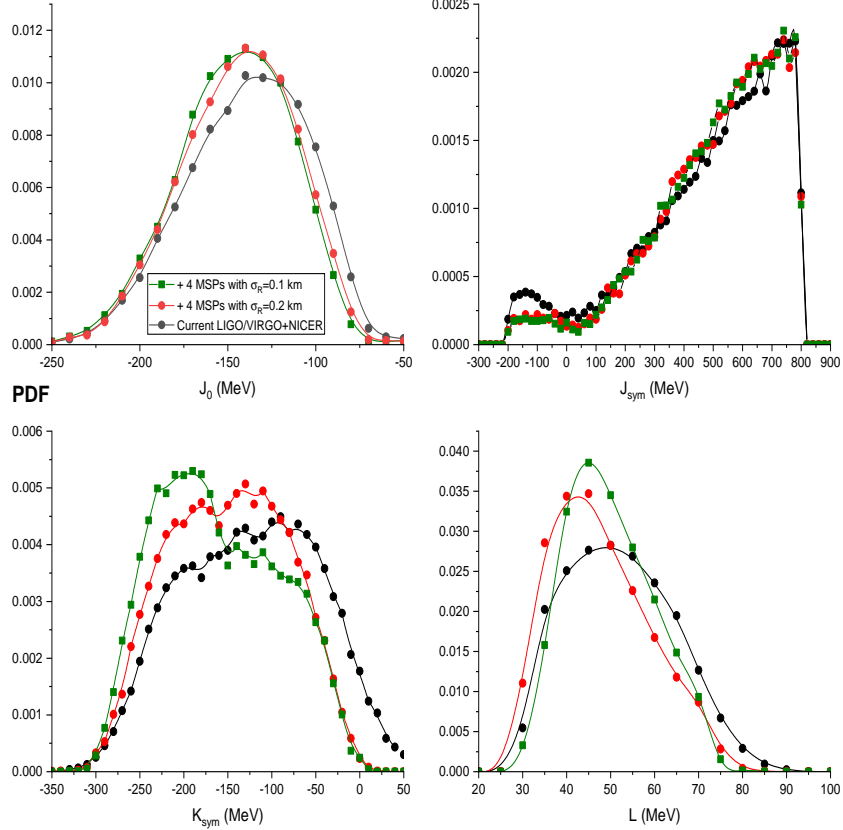


FIG. 14: (color online) Posterior PDFs of the four key EOS parameters obtained from including the mass and radius data of the four MSPs listed in Table II with the expected precision of $\Delta R = 0.2$ km and 0.1 km, respectively, with respect to the results obtained from using only the radius data from GW170817 by LIGO/VIRGO, as well as those for PSR J0030+0451 and PSR J0740+6620 from NICER listed also in Table II.

same mass but different radii [81] and fine features of nuclear EOS [82]. Actually, one possible reason for the non-detection of twin stars so far is that their radius separation predicted with most EOSs are mostly less than the best precision ΔR of present NS radius measurements [83].

Listed in the last 4 rows in Table II are four MSPs with precisely measured masses between about 1.2 to $2 M_{\odot}$. Their presently known radii are about 1.0 km apart at the corners of a rotated \mathcal{Z} curve as shown in Fig. 1. Their radii are not well constrained according to Refs. [1, 66–69]. The differences between their radii are at the same level as the current best precision $\Delta R \approx 1.0$ km. Since these four MSPs cover approximately the same mass range as the case we studied in the previous subsection assuming $R_{1.4} = R_{1.6} = R_{1.8} = R_{2.0} = 11.9$ km with a varying precision, a comparative study here with high precision simultaneously for all four MSPs is at least educational. We will also compare the results from this study with the ones (used as a reference below) obtained from

using only the data from GW170817 by LIGO/VIRGO, as well as the PSR J0030+0451 and PSR J0740+6620 data from NICER listed in Table II.

Our results are shown in Fig. 14. It is seen that the $\text{PDF}(J_0)$ shifts towards a slightly lower MPV of J_0 around -150 MeV with both $\Delta R = 0.1$ and 0.2 km compared to the reference from using the combined data from LIGO/VIRGO+NICER. This is consistent with our findings in the previous subsections. The $\text{PDF}(J_{\text{sym}})$ does not seem to show any difference mostly due to the mixing of the radius data of four MSPs on the \mathcal{Z} curve. Similarly, the situation holds for L , although one can still distinguish its PDF obtained with different precision. On the other hand, since K_{sym} is the parameter most sensitive to the variation of NS radii, its PDF shows some structures. Again, these structures at high precision are due to the anti-correlations of K_{sym} with J_{sym} and L . The relative heights of the two-peaks (or a peak and a shoulder) depend sensitively on the precision ΔR as the latter affects strongly different contributions to the total like-

likelihood function from the four MSPs when the EOSs are sampled during the MCMC process. Obviously, because of the mixing of NS radius data about 1.0 km apart, the effects of the precision are not as clear as in the previous case when all four NSs are assumed to have the same radius.

IV. SUMMARY AND CONCLUSIONS

In summary, future high-precision X-ray and gravitational wave observatories are designed to measure NS radii with unprecedented precision. Some recent analyses and simulations have forecasted that a network consisting of one Cosmic Explorer and the Einstein Telescope can measure the radii of NSs in the mass range of $(1.0 - 2.0) M_{\odot}$ with an accuracy $\sigma_R \equiv \Delta R$ less than 0.1 km that is more than ten times better than current constraints from LIGO-Virgo-KAGRA and NICER. One outstanding scientific goal of these high-precision radius measurements is to constrain more precisely the nuclear EOS. However, other than the stiffness generally spoken of in the literature, it is presently unclear what particular aspects of the EOS and to what precision they will be better constrained by the proposed high-precision NS radius measurements.

Within a Bayesian framework using a meta-model EOS for NSs consisting of $npe\mu$ matter at β -equilibrium, we inferred systematically the PDFs and pairwise correlations of the EOS parameters using several imagined data sets. We found that some interesting fine-features of the EOS of superdense neutron-rich matter can be extracted from the expected high-precision NS radius data. In particular, we found that (1) the precision ΔR of measuring NS radii has little effect on inferring the SNM stiffness (in terms of its incompressibility K_0 and skewness J_0 measuring the stiffness of SNM around ρ_0 and $(3 - 4)\rho_0$, respectively), (2) NS radius measurements with higher precision reveal more accurately not only the PDFs of but also pairwise correlations among parameters characterizing the high-density behavior of nuclear symmetry energy $E_{\text{sym}}(\rho)$, (3) the PDF of curvature K_{sym} has two peaks corresponding to its strong anti-correlations with the slope L and skewness J_{sym} of $E_{\text{sym}}(\rho)$ when

ΔR in measuring the radii of canonical NSs is less than about 0.2 km, (4) high-precision radius measurements for canonical NSs is more useful than massive ones for constraining the EOS of nucleonic matter at supersaturation densities. Overall, important new physics regarding the EOS of supradense neutron-rich nuclear matter can be obtained with the planned NS radius measurements with unprecedented precision.

There are certainly caveats in our work. For example, as stated clearly earlier, we used conservatively the so-called minimum model for NSs to reduce the number of model assumptions, parameters and their uncertainties. There is no doubt that high-precision NS radius measurements may help reveal other new physics when more degrees of freedom, particles and phases are considered in modeling NSs. Nevertheless, results from our present work provide a useful foundation for further exploring new physics with the expected high-precision NS radius data. We are thus enthusiastically waiting for the NS radius data with precision better than 0.1 km.

Acknowledgement: BAL and XG were supported in part by the U.S. Department of Energy, Office of Science, under Award Number DE-SC0013702, the CUSTIPEN (China-U.S. Theory Institute for Physics with Exotic Nuclei) under the US Department of Energy Grant No. DE-SC0009971, and the Office of Vice President for Research and Economic Development at Texas A&M University-Commerce. WJX was supported in part by the Shanxi Provincial Foundation for Returned Overseas Scholars under Grant No 20220037, the Natural Science Foundation of Shanxi Province under Grant No 20210302123085, the Open Project of Guangxi Key Laboratory of Nuclear Physics and Nuclear Technology, No. NLK2023-03 and the Central Government Guidance Funds for Local Scientific and Technological Development, China (No. Guike ZY22096024). NBZ is supported in part by the National Natural Science Foundation of China under Grant No. 12375120, the Zhishan Young Scholar of Southeast University under Grant No. 2242024RCB0013 and the Start-up Research Fund of Southeast University under Grant No. RF1028623060.

-
- [1] A.L. Watts, et al., Dense matter with eXTP. *Sci. China Phys. Mech. Astron.* **62**, 29503 (2019). doi:10.1007/s11433-017-9188-4
 - [2] B.S. Sathyaprakash, A. Buonanno, L. Lehner, et al., Extreme gravity and fundamental physics. 2020 *Astron. Astrophys. Decadal Surv.* . arXiv:1903.09221
 - [3] S. Bogdanov, et al., Determining the Equation of State of Cold, Dense Matter with X-ray Observations of Neutron Stars. *Bull. AAS* . arXiv:1903.04648
 - [4] L. Baiotti, Gravitational waves from neutron star mergers and their relation to the nuclear equation of state. *Prog. Part. Nucl. Phys.* **109**, 103714 (2019). doi:https://doi.org/10.1016/j.pnnp.2019.103714
 - [5] B.A. Li, B.J. Cai, W.J. Xie, et al., Progress in Constraining Nuclear Symmetry Energy Using Neutron Star Observables Since GW170817. *Universe* **7**, 182 (2021). arXiv:2105.04629, doi:10.3390/universe7060182
 - [6] A. Sorensen, et al., Dense nuclear matter equation of state from heavy-ion collisions. *Prog. Part. Nucl. Phys.* **134**, 104080 (2024). arXiv:2301.13253, doi:10.1016/j.pnnp.2023.104080
 - [7] A. Lovato, et al., Long range plan: Dense matter theory

- for heavy-ion collisions and neutron stars. arXiv e-prints . arXiv:2211.02224
- [8] R. Kumar, et al., Theoretical and experimental constraints for the equation of state of dense and hot matter. *Living Rev. Rel.* **27**, 3 (2024). arXiv:2303.17021, doi:10.1007/s41114-024-00049-6
- [9] J.M. Lattimer, M. Prakash, Neutron star structure and the equation of state. *Astrophys. J.* **550**, 426 (2001). arXiv:astro-ph/0002232, doi:10.1086/319702
- [10] B.A. Li, P.G. Krastev, D.H. Wen, et al., Towards Understanding Astrophysical Effects of Nuclear Symmetry Energy. *Eur. Phys. J. A* **55**, 117 (2019). arXiv:1905.13175, doi:10.1140/epja/i2019-12780-8
- [11] E.E. Kolomeitsev, D.N. Voskresensky, The NICER data and a σ -field dependent stiffness of the hadronic equation of state. arXiv e-prints . arXiv:2404.09875
- [12] S.N. Zhang, et al., The enhanced X-ray Timing and Polarimetry mission—eXTP. *Sci. China Phys. Mech. Astron.* **62**, 29502 (2019). arXiv:1812.04020, doi:10.1007/s11433-018-9309-2
- [13] P.S. Ray, et al., STROBE-X: X-ray Timing and Spectroscopy on Dynamical Timescales from Microseconds to Years. *Rep.* . arXiv:1903.03035
- [14] S. Hild, S. Chelkowski, A. Freise, et al., A Xylophone Configuration for a third Generation Gravitational Wave Detector. *Cl. Quant. Grav.* **27**, 015003 (2010). arXiv:0906.2655, doi:10.1088/0264-9381/27/1/015003
- [15] R. Abbott, et al., GW190814: Gravitational Waves from the Coalescence of a 23 Solar Mass Black Hole with a 2.6 Solar Mass Compact Object. *Astrophys. J. Lett.* **896**, L44 (2020). arXiv:2006.12611, doi:10.3847/2041-8213/ab960f
- [16] B. Sathyaprakash, et al., Scientific Objectives of Einstein Telescope. *Cl. Quant. Grav.* **29**, 124013 (2012). [Erratum: *Class. Quant. Grav.* **30**, 079501 (2013)]. arXiv:1206.0331, doi:10.1088/0264-9381/29/12/124013
- [17] M. Evans, et al., A Horizon Study for Cosmic Explorer: Science, Observatories, and Community. *Rep.* . arXiv:2109.09882
- [18] K. Chatziioannou, Uncertainty limits on neutron star radius measurements with gravitational waves. *Phys. Rev. D* **105**, 084021 (2022). arXiv:2108.12368, doi:10.1103/PhysRevD.105.084021
- [19] C. Pacilio, A. Maselli, M. Fasano, et al., Ranking Love Numbers for the Neutron Star Equation of State: The Need for Third-Generation Detectors. *Phys. Rev. Lett.* **128**, 101101 (2022). arXiv:2104.10035, doi:10.1103/PhysRevLett.128.101101
- [20] A. Bandopadhyay, K. Kacanja, R. Somasundaram, et al., Measuring Neutron Star Radius with second and third generation Gravitational Wave Detector Networks. arXiv e-prints . arXiv:2402.05056
- [21] D. Finstad, L.V. White, D.A. Brown, Prospects for a Precise Equation of State Measurement from Advanced LIGO and Cosmic Explorer. *Astrophys. J.* **955**, 45 (2023). arXiv:2211.01396, doi:10.3847/1538-4357/acf12f
- [22] K. Walker, R. Smith, E. Thrane, et al., Precision constraints on the neutron star equation of state with third-generation gravitational-wave observatories. arXiv e-prints . arXiv:2401.02604
- [23] B.A. Li, A.W. Steiner, Constraining the radii of neutron stars with terrestrial nuclear laboratory data. *Phys. Lett. B* **642**, 436–440 (2006). arXiv:nucl-th/0511064, doi:10.1016/j.physletb.2006.09.065
- [24] B.A. Li, L.W. Chen, C.M. Ko, Recent Progress and New Challenges in Isospin Physics with Heavy-Ion Reactions. *Phys. Rept.* **464**, 113–281 (2008). arXiv:0804.3580, doi:10.1016/j.physrep.2008.04.005
- [25] J. Richter, B.A. Li, Empirical radius formulas for canonical neutron stars from bidirectionally selecting features of equations of state in extended Bayesian analyses of observational data. *Phys. Rev. C* **108**, 055803 (2023). arXiv:2307.05848, doi:10.1103/PhysRevC.108.055803
- [26] FRIB Science Community, *FRIB 400 white paper: The Scientific Case for the 400 MeV/u Energy Upgrade of Facility for Rare Isotope Beam Facility (FRIB)*, (Facility for Rare Isotope Beams, 2019). doi:https://fribusers.org/documents/2019/FRIB400-Upgrade.pdf
- [27] D. Almaalol, et al., QCD Phase Structure and Interactions at High Baryon Density: Continuation of BES Physics Program with CBM at FAIR. arXiv e-prints . arXiv:2209.05009
- [28] L.W. Chen, X. Dong, K. Fukushima, et al., *Nuclear Matter at High Density and Equation of State*, (Springer Nature Singapore, Singapore, 2022), pp. 183–285. doi:10.1007/978-981-19-4441-3_4
- [29] N.B. Zhang, B.A. Li, J. Xu, Combined constraints on the equation of state of dense neutron-rich matter from terrestrial nuclear experiments and observations of neutron stars. *The Astrophys. J.* **859**, 90 (2018). doi:10.3847/1538-4357/aac027
- [30] N.B. Zhang, B.A. Li, Implications of the Mass $M = 2.17_{-0.10}^{+0.11}M_{\odot}$ of PSR J0740+6620 on the Equation of State of Super-dense Neutron-rich Nuclear Matter. *Astrophys. J.* **879**, 99 (2019). arXiv:1904.10998, doi:10.3847/1538-4357/ab24cb
- [31] N.B. Zhang, B.A. Li, Impact of NICER’s Radius Measurement of PSR J0740+6620 on Nuclear Symmetry Energy at Suprasaturation Densities. *Astrophys. J.* **921**, 111 (2021). arXiv:2105.11031, doi:10.3847/1538-4357/ac1e8c
- [32] W.J. Xie, B.A. Li, Bayesian inference of high-density nuclear symmetry energy from radii of canonical neutron stars. *The Astrophys. J.* **883**, 174 (2019). doi:10.3847/1538-4357/ab3f37
- [33] W.J. Xie, B.A. Li, Bayesian inference of the symmetry energy of superdense neutron-rich matter from future radius measurements of massive neutron stars. *The Astrophys. J.* **899**, 4 (2020). doi:10.3847/1538-4357/aba271
- [34] W.J. Xie, B.A. Li, Bayesian inference of the dense-matter equation of state encapsulating a first-order hadron-quark phase transition from observables of canonical neutron stars. *Phys. Rev. C* **103**, 035802 (2021).
- [35] B.A. Li, P.G. Krastev, D.H. Wen, et al., Towards Understanding Astrophysical Effects of Nuclear Symmetry Energy. *Eur. Phys. J. A* **55**, 117 (2019). arXiv:1905.13175, doi:10.1140/epja/i2019-12780-8
- [36] I. Bombaci, U. Lombardo, Asymmetric nuclear matter equation of state. *Phys. Rev. C* **44**, 1892 (1991).
- [37] J.R. Oppenheimer, G.M. Volkoff, On massive neutron cores. *Phys. Rev.* **55**, 374 (1939).
- [38] J.M. Lattimer, M. Prakash, Neutron Star Observations: Prognosis for Equation of State Constraints. *Phys. Rept.* **442**, 109–165 (2007). arXiv:astro-ph/0612440, doi:10.1016/j.physrep.2007.02.003
- [39] S. Kubis, Nuclear symmetry energy and stability of matter in neutron stars. *Phys. Rev. C* **76**, 025801 (2007).
- [40] J. Xu, L.W. Chen, B.A. Li, et al., Nuclear constraints

- on properties of neutron star crusts. *Astrophys. J.* **697**, 1549–1568 (2009). arXiv:0901.2309, doi:10.1088/0004-637X/697/2/1549
- [41] J.W. Negele, D. Vautherin, Neutron star matter at sub-nuclear densities. *Nucl. Phys. A* **207**, 298–320 (1973). doi:[https://doi.org/10.1016/0375-9474\(73\)90349-7](https://doi.org/10.1016/0375-9474(73)90349-7)
- [42] G. Baym, C. Pethick, P. Sutherland, The ground state of matter at high densities: equation of state and stellar models. *The Astrophys. J.* **170**, 299 (1971). doi:10.1086/151216
- [43] R.C. Tolman, Effect of inhomogeneity on cosmological models. *Proc. Natl. Acad. Sci.* **20**, 169–176 (1934).
- [44] W.J. Xie, B.A. Li, Bayesian inference of the incompressibility, skewness and kurtosis of nuclear matter from empirical pressures in relativistic heavy-ion collisions. *J. Phys. G* **48**, 025110 (2021). arXiv:2001.03669, doi:10.1088/1361-6471/abd25a
- [45] U. Garg, G. Colò, The compression-mode giant resonances and nuclear incompressibility. *Prog. Part. Nucl. Phys.* **101**, 55–95 (2018). arXiv:1801.03672, doi:10.1016/j.pnpnp.2018.03.001
- [46] S. Shlomo, V.M. Kolomietz, G. Colò, Deducing the nuclear-matter incompressibility coefficient from data on isoscalar compression modes. *Eur. Phys. J. A* **30**, 23–30 (2006). doi:10.1140/epja/i2006-10100-3
- [47] B.A. Li, X. Han, Constraining the neutron-proton effective mass splitting using empirical constraints on the density dependence of nuclear symmetry energy around normal density. *Phys. Lett. B* **727**, 276–281 (2013). arXiv:1304.3368, doi:10.1016/j.physletb.2013.10.006
- [48] M. Oertel, M. Hempel, T. Klähn, et al., Equations of state for supernovae and compact stars. *Rev. Mod. Phys.* **89**, 015007 (2017). arXiv:1610.03361, doi:10.1103/RevModPhys.89.015007
- [49] B.A. Li, Nuclear Symmetry Energy Extracted from Laboratory Experiments. *Nucl. Phys. News* **27**, 7–11 (2017). arXiv:1701.03564, doi:10.1080/10619127.2017.1388681
- [50] C. Mondal, B.K. Agrawal, J.N. De, et al., Interdependence of different symmetry energy elements. *Phys. Rev. C* **96**, 021302 (2017). arXiv:1708.03846, doi:10.1103/PhysRevC.96.021302
- [51] J. Margueron, R. Hoffmann Casali, F. Gulminelli, Equation of state for dense nucleonic matter from meta-modeling. II. Predictions for neutron star properties. *Phys. Rev. C* **97**, 025806 (2018). arXiv:1708.06895, doi:10.1103/PhysRevC.97.025806
- [52] R. Somasundaram, C. Drischler, I. Tews, et al., Constraints on the nuclear symmetry energy from asymmetric-matter calculations with chiral NN and $3N$ interactions. *Phys. Rev. C* **103**, 045803 (2021). arXiv:2009.04737, doi:10.1103/PhysRevC.103.045803
- [53] G. Grams, R. Somasundaram, J. Margueron, et al., Nuclear incompressibility and speed of sound in uniform matter and finite nuclei. *Phys. Rev. C* **106**, 044305 (2022). arXiv:2207.01884, doi:10.1103/PhysRevC.106.044305
- [54] B.J. Cai, L.W. Chen, Constraints on the skewness coefficient of symmetric nuclear matter within the nonlinear relativistic mean field model. *Nucl. Sci. Tech.* **28**, 185 (2017). arXiv:1402.4242, doi:10.1007/s41365-017-0329-1
- [55] N.B. Zhang, B.J. Cai, B.A. Li, et al., How tightly is the nuclear symmetry energy constrained by a unitary Fermi gas? *Nucl. Sci. Tech.* **28**, 181 (2017). arXiv:1704.02687, doi:10.1007/s41365-017-0336-2
- [56] I. Tews, J.M. Lattimer, A. Ohnishi, et al., Symmetry Parameter Constraints from a Lower Bound on Neutron-matter Energy. *Astrophys. J.* **848**, 105 (2017). arXiv:1611.07133, doi:10.3847/1538-4357/aa8db9
- [57] L. Lindblom, Causal Representations of Neutron-Star Equations of State. *Phys. Rev. D* **97**, 123019 (2018). arXiv:1804.04072, doi:10.1103/PhysRevD.97.123019
- [58] B.A. Li, A. Ramos, G. Verde, et al., Topical issue on nuclear symmetry energy. *Eur. Phys. J. A* **50**, 9 (2014). doi:10.1140/epja/i2014-14009-x
- [59] B.J. Cai, B.A. Li, Auxiliary function approach for determining symmetry energy at suprasaturation densities. *Phys. Rev. C* **103**, 054611 (2021). arXiv:2104.02185, doi:10.1103/PhysRevC.103.054611
- [60] B.P. Abbott, R. Abbott, T. Abbott, et al., Gw170817: Measurements of neutron star radii and equation of state. *Phys. review letters* **121**, 161101 (2018). doi:10.1103/PhysRevLett.121.161101
- [61] S. De, D. Finstad, J.M. Lattimer, et al., Tidal deformabilities and radii of neutron stars from the observation of gw170817. *Phys. review letters* **121**, 091102 (2018). doi:10.1103/PhysRevLett.121.091102
- [62] J.M. Lattimer, A.W. Steiner, Constraints on the symmetry energy using the mass-radius relation of neutron stars. *The Eur. Phys. J. A* **50**, 1–24 (2014). doi:<https://doi.org/10.1140/epja/i2014-14040-y>
- [63] T.E. Riley, A.L. Watts, S. Bogdanov, et al., A nicer view of psr j0030+ 0451: millisecond pulsar parameter estimation. *The Astrophys. J. Lett.* **887**, L21 (2019). doi:10.3847/2041-8213/ab481c
- [64] M.C. Miller, et al., PSR J0030+0451 Mass and Radius from *NICER* Data and Implications for the Properties of Neutron Star Matter. *Astrophys. J. Lett.* **887**, L24 (2019). arXiv:1912.05705, doi:10.3847/2041-8213/ab50c5
- [65] E. Fonseca, H.T. Cromartie, T.T. Pennucci, et al., Refined mass and geometric measurements of the high-mass psr j0740+ 6620. *The Astrophys. J. Lett.* **915**, L12 (2021). doi:10.3847/2041-8213/ac03b8
- [66] D.J. Nice, et al., in 40 years of pulsars: Millisecond pulsars, magnetars and more. *AIP Conf. Proc.*, 983, 453 .
- [67] N.A. Webb, D. Leahy, S. Guillot, et al., Thermal X-ray emission identified from the millisecond pulsar PSR J1909–3744. *Astron. Astrophys.* **627**, A141 (2019). arXiv:1906.10438, doi:10.1051/0004-6361/201732040
- [68] Y.J. Guo, et al., PSR J2222–0137 - I. Improved physical parameters for the system. *Astron. Astrophys.* **654**, A16 (2021). arXiv:2107.09474, doi:10.1051/0004-6361/202141450
- [69] Z. Arzoumanian, et al., The NANOGrav 11-year Data Set: High-precision timing of 45 Millisecond Pulsars. *Astrophys. J. Suppl.* **235**, 37 (2018). arXiv:1801.01837, doi:10.3847/1538-4365/aab5b0
- [70] B.P. Abbott, R. Abbott, T. Abbott, et al., Gw170817: observation of gravitational waves from a binary neutron star inspiral. *Phys. review letters* **119**, 161101 (2017).
- [71] N.B. Zhang, B.A. Li, GW190814’s Secondary Component with Mass $2.50\text{--}2.67 M_{\odot}$ as a Superfast Pulsar. *Astrophys. J.* **902**, 38 (2020). arXiv:2007.02513, doi:10.3847/1538-4357/abb470
- [72] R. Trotta, Bayesian methods in cosmology. arXiv preprint arXiv:1701.01467 . doi:<https://doi.org/10.48550/arXiv.1701.01467>
- [73] N. Turkkan, T. Pham-Gia, Computation of the highest posterior density interval in

- bayesian analysis. *Stat. Comput. Sim.* **44**,
doi:<https://doi.org/10.1080/00949659308811461>
- [74] J.M. Lattimer, M. Prakash, C.J. Pethick, et al., Direct URCA process in neutron stars. *Phys. Rev. Lett.* **66**, 2701–2704 (1991). doi:[10.1103/PhysRevLett.66.2701](https://doi.org/10.1103/PhysRevLett.66.2701)
- [75] T. Klahn, et al., Constraints on the high-density nuclear equation of state from the phenomenology of compact stars and heavy-ion collisions. *Phys. Rev. C* **74**, 035802 (2006). arXiv:[nucl-th/0602038](https://arxiv.org/abs/nucl-th/0602038), doi:[10.1103/PhysRevC.74.035802](https://doi.org/10.1103/PhysRevC.74.035802)
- [76] L. Shi, P. Danielewicz, Effect of cluster formation on isospin asymmetry in the liquid gas phase transition region. *EPL* **49**, 34–40 (2000). arXiv:[nucl-th/0002065](https://arxiv.org/abs/nucl-th/0002065), doi:[10.1209/epl/i2000-00116-1](https://doi.org/10.1209/epl/i2000-00116-1)
- [77] N.B. Zhang, B.A. Li, Impact of symmetry energy on sound speed and spinodal decomposition in dense neutron-rich matter. *Eur. Phys. J. A* **59**, 86 (2023). arXiv:[2208.00321](https://arxiv.org/abs/2208.00321), doi:[10.1140/epja/s10050-023-01010-x](https://doi.org/10.1140/epja/s10050-023-01010-x)
- [78] O. Boukari, T. Malik, A. Rabhi, et al., Constraining the high-density behavior of nuclear symmetry energy with direct Urca processes. to be published. . arXiv:[2407.04403](https://arxiv.org/abs/2407.04403)
- [79] N.B. Zhang, B.A. Li, Extracting Nuclear Symmetry Energies at High Densities from Observations of Neutron Stars and Gravitational Waves. *Eur. Phys. J. A* **55**, 39 (2019). arXiv:[1807.07698](https://arxiv.org/abs/1807.07698), doi:[10.1140/epja/i2019-12700-0](https://doi.org/10.1140/epja/i2019-12700-0)
- [80] Y.Z. Fan, M.Z. Han, J.L. Jiang, et al., Maximum gravitational mass $M_{\text{TOV}}=2.25-0.07+0.08M_{\odot}$ inferred at about 3% precision with multimessenger data of neutron stars. *Phys. Rev. D* **109**, 043052 (2024). arXiv:[2309.12644](https://arxiv.org/abs/2309.12644), doi:[10.1103/PhysRevD.109.043052](https://doi.org/10.1103/PhysRevD.109.043052)
- [81] M.G. Alford, S. Han, M. Prakash, Generic conditions for stable hybrid stars. *Phys. Rev. D* **88**, 083013 (2013). arXiv:[1302.4732](https://arxiv.org/abs/1302.4732), doi:[10.1103/PhysRevD.88.083013](https://doi.org/10.1103/PhysRevD.88.083013)
- [82] M. Ferreira, C. Providência, Constraining neutron star matter from dM/dR . To be published . arXiv:[2406.12582](https://arxiv.org/abs/2406.12582)
- [83] N.B. Zhang, B.A. Li, Impact of the nuclear equation of state on the formation of twin stars. To be published . arXiv:[2406.07396](https://arxiv.org/abs/2406.07396)